

University of Southern Queensland
Faculty of Health, Engineering & Sciences

3D Simulation of Submerged Plates

A dissertation submitted by

S. Anderson

in fulfilment of the requirements of

ENG4111 / 4112 Research Project

towards the degree of

Bachelor of Engineering (Mechanical)

Submitted: October, 2023

Abstract

Linear Energy Harvesters are a type of hydro generator that are applicable to shallow, low velocity, open channel flows. These types of generators are driven by arrays of shallowly submerged plates. B. Attiya et al. performed Large Eddy Simulations of shallowly submerged plates of varying aspect ratio to analyse the performance of the plates in a multiphase open channel flow. This research project aims to build on their previous works and to improve the performance of the plates by increasing the plates co-efficient of drag.

ANSYS Fluent was used to model the plates for Computational Fluid Dynamics analysis. The projects first aim was to validate the model against the works of B. Attiya using a Reynolds Averaged Navier-Stokes method. A curved profile was then added to the plates for analysis and the purpose of comparison to the flat plates.

It was found that for 250, 500, and 1000mm wide by 100mm high flat plates, by adding a 50mm radius bend to the plate the coefficients of lift and drag were increased. By adding a curve to the plates the 250mm wide plate the drag was increased by 7.35%, the 500mm wide plate 21.06%, and the 1000mm wide plate 6.07%. All plates experienced large increases in lift ranging from 56.3 to 67.0%. It was shown that the curve affected the manner of vortex shedding, with turbulent flows running down the entire rear face of the curved plates.

ENG4111/2 <i>Research Project</i>
--

Limitations of Use

The Council of the University of Southern Queensland, its Faculty of Health, Engineering & Sciences, and the staff of the University of Southern Queensland, do not accept any responsibility for the truth, accuracy or completeness of material contained within or associated with this dissertation.

Persons using all or any part of this material do so at their own risk, and not at the risk of the Council of the University of Southern Queensland, its Faculty of Health, Engineering & Sciences or the staff of the University of Southern Queensland.

This dissertation reports an educational exercise and has no purpose or validity beyond this exercise. The sole purpose of the course pair entitled “Research Project” is to contribute to the overall education within the student’s chosen degree program. This document, the associated hardware, software, drawings, and other material set out in the associated appendices should not be used for any other purpose: if they are so used, it is entirely at the risk of the user.

Dean

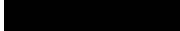
Faculty of Health, Engineering & Sciences

Certification of Dissertation

I certify that the ideas, designs and experimental work, results, analyses and conclusions set out in this dissertation are entirely my own effort, except where otherwise indicated and acknowledged.

I further certify that the work is original and has not been previously submitted for assessment in any other course or institution, except where specifically stated.

S. ANDERSON

A solid black rectangular box used to redact the signature of the author.

Acknowledgments

I would like to acknowledge my supervisor Dr. Khalid Saleh for being generous with his time, support, and sharing his wealth of knowledge and expertise. I would also like to acknowledge the University of Southern Queensland for the years of education and resources that have helped me reach this point in my academic development. Finally I would like to thank my family for their patience, love, and support.

S. ANDERSON

Contents

Abstract	i
Acknowledgments	iv
List of Figures	ix
List of Tables	xii
Chapter 1 Introduction	1
1.1 Project Objectives	2
1.2 Overview of the Dissertation	2
Chapter 2 Background Information	5
2.1 Chapter Overview	5
2.2 Fluid Mechanics Concepts	5
2.2.1 Flow Characterisation	6
2.2.2 Boundary Layers	7
2.3 Open Channel Flow	8
2.4 Equations of Motion	9

2.5	Project Motivation	11
Chapter 3 Literature Review		13
3.1	Chapter Overview	13
3.2	Computational Fluid Dynamics	13
3.2.1	Finite Volume Method	15
3.3	Turbulence Models	17
3.3.1	Reynolds Averaged Navier-Stokes	19
3.3.2	Large Eddy Simulations	21
3.4	Meshing Quality	23
3.5	Initial and Boundary Conditions	24
3.6	Volume of Fluids	25
3.7	Validation of CFD Modelling	26
3.8	Coherent Structures	28
3.9	Chapter Summary	29
Chapter 4 Model Validation		31
4.1	Chapter Overview	31
4.2	Previous Works	31
4.3	Validation Simulation Setup	33
4.4	Validation Results	35
4.5	Chapter Summary	36

Chapter 5	Domain Size and Mesh Sensitivity	37
5.1	Chapter Overview	37
5.2	Domain Size Testing	37
5.3	Mesh Sensitivity	39
5.4	Chapter Summary	40
Chapter 6	CFD Simulation Setup	41
6.1	Chapter Overview	41
6.2	Plate and Domain Geometry	41
6.3	Hex Dominant Mesh Steady Simulation	42
6.4	Hex Dominant Mesh Transient Simulation	44
6.5	Revised Polyhedral Meshing	44
6.6	Chapter Summary	45
Chapter 7	Results	47
7.1	Chapter Overview	47
7.2	Flat Plates - Full Polyhedral Mesh Model	47
7.2.1	Flat Plates - Full Polyhedral Mesh Results	49
7.3	Curved Plates - Full Polyhedral Mesh Model	51
7.3.1	Curved Plates - Full Polyhedral Mesh Plate Forces	52
7.4	Hex Dominant Mesh Model	56
7.4.1	Hex Dominant Mesh Results	57

7.5	Transient Model Hex Dominant Mesh Results	58
7.5.1	Transient Plate Forces	58
7.6	Chapter Summary	60
Chapter 8	Results	61
8.1	Chapter Overview	61
8.2	Flat Plate Results vs B. Attiya	61
8.3	Flat vs Curved Plates	63
8.4	Steady State vs Transient 250W Flat Plate	64
8.5	Chapter Summary	64
Chapter 9	Conclusions and Further Work	67
9.1	Conclusions	67
9.2	Further Work	68
9.3	Project Self-Assessment	69
References		71
Appendix A	Project Specification	75
Appendix B	Project Plan	77
Appendix C	Revised Project Plan	79
Appendix D	B. Attiya et al. 2019 Drag Results	81

List of Figures

2.1	Viscous Flow	6
2.2	Lamninar and Turbulent Flow	7
2.3	Subcritical and Supercritical Flows	9
3.1	Discretization Techniques	14
3.2	Discrete Element Conservation	16
3.3	CFD Turbulence Solvers	18
3.4	RANS vs LES vs DNS	19
3.5	LES Size Filtering Visualisation	21
3.6	Coherent Structure Diagram	28
4.1	OpenFOAM Simulation Geometry	32
4.2	Validation Mesh	34
4.3	Validation Mesh Refinement	34
5.1	Domain Size Test	38
5.2	Domain Size Test	39

6.1	Curved plate profile and domain geometry	42
6.2	Cross section of hex dominant mesh	43
7.1	Z Axis View - Flow Characteristics of 250W Flat Plate	48
7.2	Y Axis View - Flow Characteristics of 250W Flat Plate	49
7.3	Z Axis View - Flow Characteristics of 500W Flat Plate	49
7.4	Y Axis View - Flow Characteristics of 500W Flat Plate	50
7.5	Z Axis View - Flow Characteristics of 1000W Flat Plate	50
7.6	Y Axis View - Flow Characteristics of 1000W Flat Plate	51
7.7	Z Axis View - Flow Characteristics of 250W Curved Plate	52
7.8	Y Axis View - Flow Characteristics of 250W Curved Plate	52
7.9	Z Axis View - Flow Characteristics of 500W Curved Plate	53
7.10	Y Axis View - Flow Characteristics of 500W Curved Plate	53
7.11	Z Axis View - Flow Characteristics of 1000W Curved Plate	54
7.12	Y Axis View - Flow Characteristics of 1000W Curved Plate	54
7.13	False Vorticity	56
7.14	Z Axis View - Flow Characteristics of Hex Dominant Mesh	57
7.15	Y Axis View - Flow Characteristics of Hex Dominant Mesh	57
7.16	Transient Solver Flow Characteristics of 250W Curved Plate - Z Axis View	59
7.17	Transient Solver Flow Characteristics of 250W Curved Plate - Y Axis View	59
7.18	Transient 250W Curved Plate - Drag vs Time	60

8.1	Comparison of phases	62
8.2	Curved vs Flat Plate Vorticity	64
D.1	Drag results from (Attiya, Altimemy, Caspar, Daskiran, Liu & Oztekin 2019)	81

List of Tables

2.1	Energy densities of various sources adopted from (Layton 2008).	11
3.1	RANS Model Categorisation	20
4.1	Input parameters used in OpenFOAM LES simulation adopted from (Attiya et al. 2019).	33
4.2	Comparison of results from the validation simulation.	35
5.1	Results of domain width test.	38
5.2	Results of domain length test.	38
5.3	Results of mesh sensitivity test.	39
7.1	Flat plates with full polyhedral mesh results.	51
7.2	Curved plates with full polyhedral mesh results.	55
7.3	250 wide plate results with Hex dominant mesh.	58
7.4	250 wide curved plate results from transient solver.	60
8.1	Flat vs Curved plate forces comparison.	63

Chapter 1

Introduction

Flows and their interactions with objects and structures has been an area of interest to engineers from early civilisation to the modern day. Engineers have always been intuitively drawn to the kinetic energy available in the natural flows of the environment. Harnessing the kinetic energy available in naturally occurring flows has become a critical area of study in regards to the current state of climate change and government and economic drivers towards renewable energy sources. These technologies include both wind and hydro dynamic applications of energy harvesting devices.

Naturally occurring flows that occur in water bodies are free surface by nature which are inherently difficult to analyse as the free surface can deform infinitely and is variable in height. The focus of this research paper is to consider a plate design that is shallowly submerged in a multiphase flow as an approximation of a linear energy harvester device. An evaluation of the vortical flow structures and the hydrodynamic loads on the plate shall be completed utilising the ANSYS Fluent software package. Previous works have been completed using OpenFOAM by (Attiya et al. 2019) which will be used for validation works. This research project looks to increase the performance of the submerged plate by modifying the plate geometry and analysing it's effects on the coefficient of drag.

1.1 Project Objectives

The objectives of this dissertation is to investigate the methods of CFD, validate a fluid domain and simulation, and optimise plate geometry in the domain to optimise drag performance. The project specification in Appendix A was developed at the beginning of the project and outlines the objectives of the research project. These objectives have developed as the project has progressed and are formed into the following sections:

- discuss fluid mechanics concepts
- investigate computational fluid dynamics and the finite volume method
- validate ANSYS model against previous CFD works
- simulate shallowly submerged plates of different geometrical designs
- refine mesh and plate geometry to find optimum drag coefficient
- present analysis results and propose final plate design
- evaluate research methodology and identify required areas of further research

The original planning, timing, and steps to achieve the objectives of the project can be found in Appendix B. Due to external factors this planning had to be updated for an abbreviated study period found in Appendix C.

1.2 Overview of the Dissertation

This dissertation is organised as follows:

Chapter 1 research project introduction

Chapter 2 discusses the required background information and topics pertinent to the research paper, and describes the motivation for the project

Chapter 3 is a literature review of Computational Fluid Dynamic methods and parameters, and a discussion of previous works that validate CFD

Chapter 4 describes the process of validating the ANSYS Fluent models used in the research paper

Chapter 5 presents the domain and mesh sensitivity studies

Chapter 6 outlines the plate design, domain, meshing, and simulation parameters for analysing drag force on and flows around the finite plate

Chapter 7 delivers the results from the simulations

Chapter 8 is a discussion and comparison of the results

Chapter 9 summarises and concludes the dissertation with suggestions for topics of more research and a critical self review

Chapter 2

Background Information

2.1 Chapter Overview

This chapter provides the information on background topics that are core to the understanding of this paper. It includes introductory information on the fluid mechanics concepts, open channel flow, and fluid equations of motion. The chapter concludes with the motivation for the project.

2.2 Fluid Mechanics Concepts

Fluid mechanics is an extremely broad subject that covers everything from hypersonic flight to the lubrication of mechanical parts. Despite the wide range of applications there are five basic laws which are applicable to to any fluid (Pritchard 2013).

1. The conservation of mass
2. Newton's second law of motion
3. The principle of angular momentum
4. The first law of thermodynamics
5. The second law of thermodynamics

It is from these laws that most of the equations of fluid mechanics are derived.

2.2.1 Flow Characterisation

In Continuum Fluid Mechanics flows can be characterised as either Inviscid or Viscous. Inviscid flows have nil or negligible friction, while Viscous flows have significant frictional forces. The flows considered in this paper are viscous in nature. In viscous flows that pass around an object, the flow velocity increases as it begins passing around the front of an object. There is a subsequent decrease of velocity as it flows around back of the object, at which point the flow path may separate from the object creating a low pressure, highly turbulent wake behind the object. Figure 2.1 below shows how the geometry of an object influences the extent of separation. In 2.1 (A) the rapid decrease in flow velocity causes the flow to separate earlier than in 2.1 (B) where the streamlined geometry controls the separation point by gradually decreasing the flow velocity.

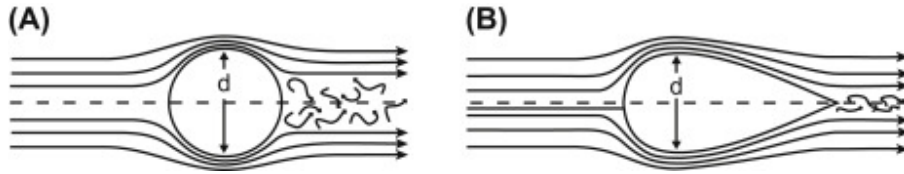


Figure 2.1: Viscous flow path around objects adapted from (Alexander 2017).

Due to the low pressure wake behind the object, there is a pressure differential across the object which creates a drag force on the object. Thus by reducing the size of the wake the figure in 2.1(B) experiences the lesser drag force.

Flows may also be described as being laminar or turbulent. In laminar flow the fluid flows in layers with no intermixing between the layers even with the existence of flow velocity profiles whereby the layers are flowing at different velocities. By contrast, turbulent flows have particles travelling in irregular paths with no definite layers, and the constantly changing velocities and direction of particles leads to energy losses. Figure 2.2 depicts the flow paths of both laminar and turbulent flows.

Whether a flow is laminar or turbulent can be determined through the calculation of the Reynolds number (Re). Reynolds number is one of the most important non-dimensional values in fluid dynamics, and is defined as the ratio of a fluids inertial forces to it's viscous shear forces (Rehm, Schubert, Haghshenas, Paknejad & Hughes 2008).

$$Re = \frac{\rho u L}{\mu} \quad (2.1)$$

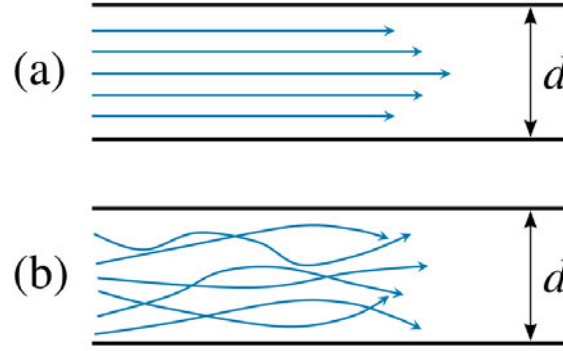


Figure 2.2: Figure a) showing laminar flow path and Figure b) turbulent flow path adapted from (SimScale 2023).

Flows in pipes with $Re < 2100$ are characterised by laminar flow, $Re > 4000$ considered fully turbulent, and flows between the two values are transitional and may randomly change between laminar and turbulent flow. In open channel this range varies greatly depending due to the introduction of more variable, as a rough guide in open channel flow $Re < 500$ is laminar and $Re > 12500$ is turbulent (Munson, Okiishi, W.Huebsch & Rothmayer 2013). Open channel water flows due to the relatively low viscosity value and large geometry are generally speaking always turbulent, for example a 3m radius channel with water at 20 degrees Celsius flowing at 0.5m/s has a Reynolds number of 1.5×10^6 . When analysing flows around a submerged object, as discussed by Munson et al. (2013) we consider the objects dimensions instead of the channels radius when calculating the Reynolds number. This leads to three Reynolds numbers, one for each dimension - height, width, and length.

2.2.2 Boundary Layers

In order to solve the Alemberts paradox from 1752, Ludwig Prandtl in 1904 theorised the existence of a boundary layer that exists around objects in inviscid flows. The velocity of the fluid at the boundary layer relative to the object is zero and increases to the velocity of the inviscid fluid as distance from the object increases. In this boundary layer the effects of friction are significant, and it is this theory that allows us to analyse drag forces on objects in inviscid flows. The size of the boundary layer is dependent on the Reynolds number with increasing values of Re having increasingly thinner boundary layers. When a boundary layer separates from an object this process is known as fluid separation (Cengel & Cimbala 2014). Boundary layers are critical to this research project as they affect the

drag force on objects that are in a fluid flow.

2.3 Open Channel Flow

Open channel flows in nature have a free surface - the boundary between the river, channel, etc. and the atmosphere, and special considerations must be given to these types of flows. As open channels are not fully confined the free surface has the ability to deform and vary in height. With the free surface at atmosphere level there is zero gauge pressure as the free surface. Gravity is the driving force in natural open channel flow (Pritchard 2013), and for this reason the effect of gravity on a system must be considered. To quantify the ratio of gravity to inertial forces another unit-less figure was defined, the Froude number (Fr).

$$Fr = \frac{V}{\sqrt{gL}} \quad (2.2)$$

The Froude number is used to determine whether an event down stream can communicate event information upstream. This can be visualised by dropping a stone into an open channel flow such as a river, illustrated in Figure 2.3.

If ripples propagate upstream and downstream with a downstream bias, i.e the wave speed is greater than the fluid speed, then $Fr < 1$ and the flow is considered subcritical. Conversely ripples that only propagate downstream have a wave speed slower than the fluid speed and $Fr > 1$ and the flow is supercritical. An even propagation of ripples upstream and downstream indicate that the fluid velocity is zero.

Froude's number is also critical in analysing hydraulic jump. When a flow transitions from a supercritical upstream flow to subcritical flow downstream the free surface height increases due to the conservation of momentum. The higher the Froude number at a hydraulic jump the greater the increase in free surface height is.

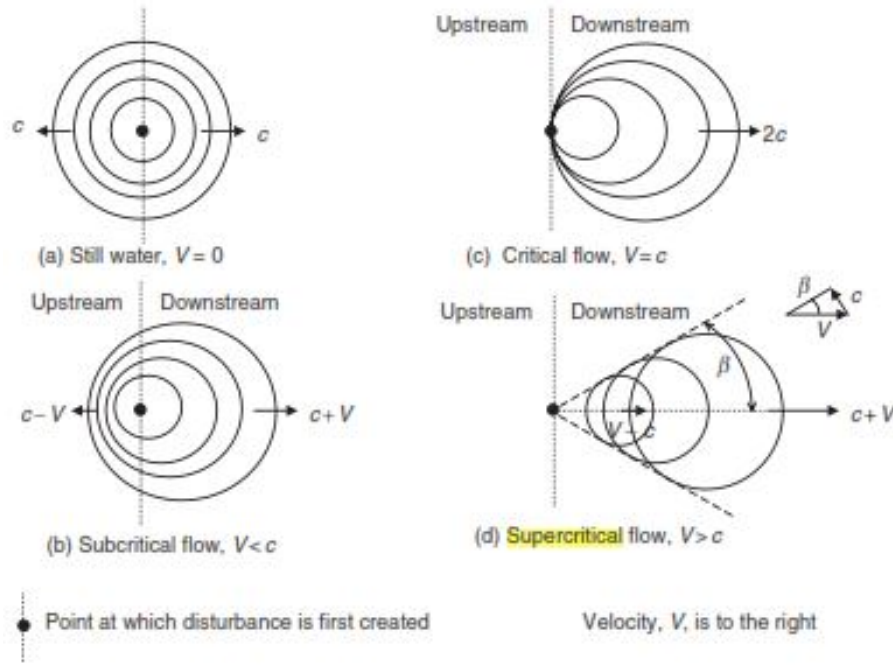


Figure 2.3: Figures a-d showing the effect of the Froude number on wave propagation adapted from (Akan 2006).

2.4 Equations of Motion

The forces and properties of a fluid flow - velocity, pressure, temperature, and density - are related (NASA 2021b). Calculating a flow problem requires five simultaneous partial derivative equations to be solved, which is known as a coupled system. These time dependent equations, based on the laws mentioned at the start of the chapter, are the Continuity Equation Eq 2.3, the Energy Equation Eq 2.4, and the Conservation of Momentum in three dimensions Eq 2.5, 2.6, and 2.7.

$$\frac{\partial(\rho u)}{\partial x} + \frac{\partial(\rho v)}{\partial y} + \frac{\partial(\rho w)}{\partial z} = 0 \quad (2.3)$$

$$\begin{aligned} \rho \frac{De}{Dt} = & \rho \dot{q} + \frac{\partial}{\partial x} \left(k \frac{\partial T}{\partial x} \right) + \frac{\partial}{\partial y} \left(k \frac{\partial T}{\partial y} \right) + \frac{\partial}{\partial z} \left(k \frac{\partial T}{\partial z} \right) \\ & - p \left(\frac{\partial u}{\partial x} + \frac{\partial v}{\partial y} + \frac{\partial w}{\partial z} \right) + \tau_{xx} \frac{\partial u}{\partial x} + \tau_{yx} \frac{\partial u}{\partial y} + \tau_{zx} \frac{\partial u}{\partial z} + \tau_{xy} \frac{\partial v}{\partial x} \\ & + \tau_{yy} \frac{\partial v}{\partial y} + \tau_{zy} \frac{\partial v}{\partial z} + \tau_{xz} \frac{\partial w}{\partial x} + \tau_{yz} \frac{\partial w}{\partial y} + \tau_{zz} \frac{\partial w}{\partial z} \end{aligned} \quad (2.4)$$

$$\begin{aligned} \rho \frac{Du}{Dt} = & \rho g_x - \frac{\partial p}{\partial x} + \frac{\partial}{\partial x} \left[\mu \left(2 \frac{\partial u}{\partial x} - \frac{2}{3} \nabla \cdot \vec{V} \right) \right] + \frac{\partial}{\partial y} \left[\mu \left(\frac{\partial u}{\partial y} + \frac{\partial v}{\partial x} \right) \right] \\ & + \frac{\partial}{\partial z} \left[\mu \left(\frac{\partial w}{\partial x} + \frac{\partial u}{\partial z} \right) \right] \end{aligned} \quad (2.5)$$

$$\begin{aligned} \rho \frac{Dv}{Dt} = & \rho g_y - \frac{\partial p}{\partial y} + \frac{\partial}{\partial x} \left[\mu \left(\frac{\partial u}{\partial y} + \frac{\partial v}{\partial x} \right) \right] + \frac{\partial}{\partial y} \left[\mu \left(2 \frac{\partial v}{\partial y} - \frac{2}{3} \nabla \cdot \vec{V} \right) \right] \\ & + \frac{\partial}{\partial z} \left[\mu \left(\frac{\partial v}{\partial z} + \frac{\partial w}{\partial y} \right) \right] \end{aligned} \quad (2.6)$$

$$\begin{aligned} \rho \frac{Dw}{Dt} = & \rho g_z - \frac{\partial p}{\partial z} + \frac{\partial}{\partial x} \left[\mu \left(\frac{\partial w}{\partial x} + \frac{\partial u}{\partial z} \right) \right] + \frac{\partial}{\partial y} \left[\mu \left(\frac{\partial w}{\partial z} + \frac{\partial w}{\partial y} \right) \right] \\ & + \frac{\partial}{\partial z} \left[\mu \left(2 \frac{\partial w}{\partial z} - \frac{2}{3} \nabla \cdot \vec{V} \right) \right] \end{aligned} \quad (2.7)$$

By substituting expressions for the stresses into the momentum equations we can derive the Navier-Stokes equations. In non-compressible flow where viscosity is constant such as those considered in this paper, the Navier-Stokes equations simplify to Eq 2.8, 2.9, and 2.10.

$$\rho \left(\frac{\partial u}{\partial t} + u \frac{\partial u}{\partial x} + v \frac{\partial u}{\partial y} + w \frac{\partial u}{\partial z} \right) = \rho g_x - \frac{\partial p}{\partial x} + \mu \left(\frac{\partial^2 u}{\partial x^2} + \frac{\partial^2 u}{\partial y^2} + \frac{\partial^2 u}{\partial z^2} \right) \quad (2.8)$$

$$\rho \left(\frac{\partial v}{\partial t} + u \frac{\partial v}{\partial x} + v \frac{\partial v}{\partial y} + w \frac{\partial v}{\partial z} \right) = \rho g_y - \frac{\partial p}{\partial y} + \mu \left(\frac{\partial^2 v}{\partial x^2} + \frac{\partial^2 v}{\partial y^2} + \frac{\partial^2 v}{\partial z^2} \right) \quad (2.9)$$

$$\rho \left(\frac{\partial w}{\partial t} + u \frac{\partial w}{\partial x} + v \frac{\partial w}{\partial y} + w \frac{\partial w}{\partial z} \right) = \rho g_z - \frac{\partial p}{\partial z} + \mu \left(\frac{\partial^2 w}{\partial x^2} + \frac{\partial^2 w}{\partial y^2} + \frac{\partial^2 w}{\partial z^2} \right) \quad (2.10)$$

Except for rare instances the Navier-Stokes equations do not have analytical exact answers, however in these cases the results are in good agreement with experimental data (Munson et al. 2013). In inviscid flows where friction is equal to zero the Navier-Stokes equations reduce to Euler's equation. Due to the complex nature of solving Navier-Stokes equations powerful computer hardware is required and software programs such as Fluent, OpenFOAM etc have been developed to tackle Computational Fluid Dynamics problems.

2.5 Project Motivation

With the current focus on climate change and renewable energy sources, engineers are focused on refining technology for the most efficient ways in which to harvest energy from nature. Liquid fluid flows in rivers and ocean waves have a high energy density that could provide significant amounts of renewable energy if harnessed efficiently. Table 2.1 shows the energy densities of various sources.

Table 2.1: Energy densities of various sources adopted from (Layton 2008).

Source	Joules per cubic meter
Solar	0.0000015
Geothermal	0.05
Wind at 10 mph (5m/s)	7
Tidal water	0.5–50
Human	1,000
Oil	45,000,000,000
Gasoline	10,000,000,000
Automobile occupied (5800 lbs)	40,000,000
Automobile unoccupied (5000 lbs)	40,000,000
Natural gas	40,000,000
Fat (food)	30,000,000

Hydro-kinetic turbines can be approximated to arrays of submerged in plates in multi-phase flow for the purpose of simplifying modelling and calculation. The motivation behind this project is to investigate the effects of plate geometry on hydrodynamic loading and maximise the drag force experienced a submerged plate. By increasing the coefficient of drag we can maximise the potential to harvest the most energy possible from the fluid flow into usable electricity.

Chapter 3

Literature Review

3.1 Chapter Overview

This chapter is a detailed investigation into the CFD tools available, turbulent flow structures, as well as previous works both experimental and computational on external flows around objects.

3.2 Computational Fluid Dynamics

Soon after the berth of modern computing came the beginning of Computational Fluid Dynamics (CFD) in the early 1970's. One of the earliest uses of CFD methods was the simulation of transonic flows based on the solutions of non-linear potential equations (Blazek 2001). With the advancement of computing and numerical acceleration first 3D Euler equations became solvable and then the more demanding Navier-Stokes equations which are now the cornerstone of CFD solvers.

All CFD solvers use a process called discretisation. This is described by Anderson (1995) as the approximation of closed-form expressions such as a partial differential equation (PDE) with analogous expressions which prescribe values at a finite number of discrete points in a given domain.

The three methods of discretisation, Finite Difference Method (FDM), Finite Volume

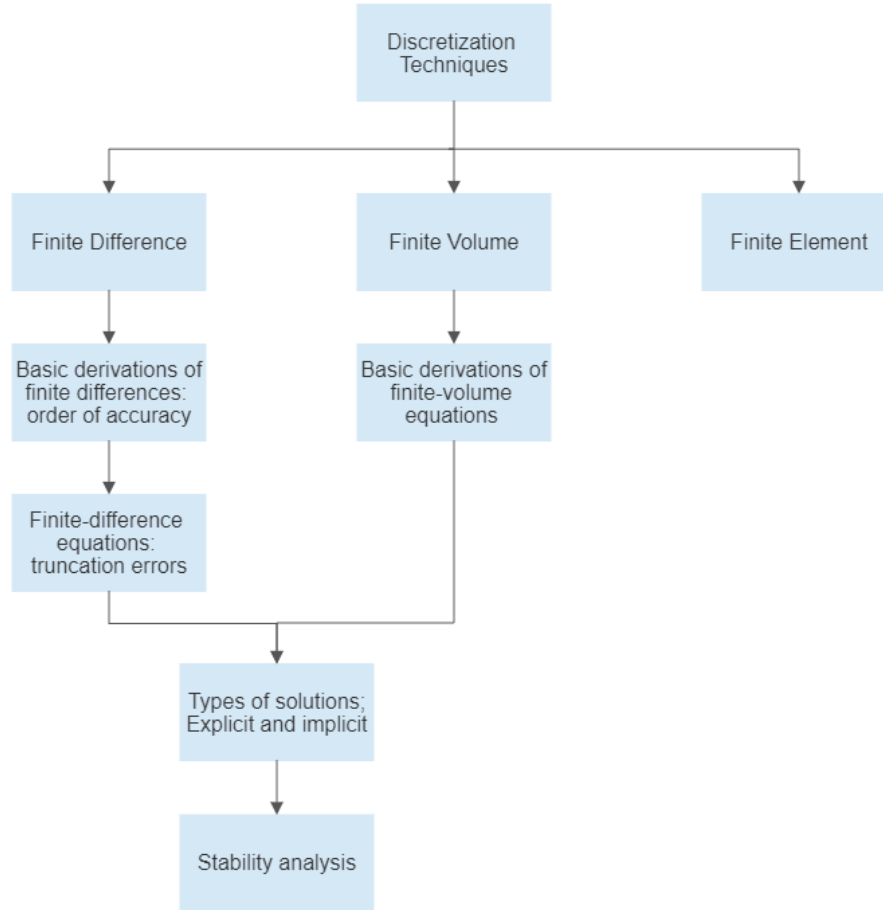


Figure 3.1: Road map of CFD analysis discretization techniques adapted from (Anderson 1995).

Method (FVM), and Finite Element Method (FEM) shown in figure 3.1 have different strengths and weaknesses. FDM approximates the complex PDEs with finite derivative equations that are analysed by performing Taylor expansions around points in the domain citePeiro2005. This is the most direct method out of the three however the grid must be regular and is not suitable for fluids where the domain is highly irregular and evolves with time.

FEM was originally used for structural analysis however can be used to solve Euler and Navier-Stokes equations in fluid flow (Blazek 2001). The domain is divided into tetrahedral 3d elements which is conducive for analysing complex geometries. FEM transforms the PDE's within each element into an integral form with a finite number of degrees of freedom. FEM provides a continuous solution as each element is assembled in a matrix of equations that assimilates the model. This requires that the initial boundary conditions of the model must be highly accurate in order to achieve accurate simulation results. FEM is computationally the most demanding of the methods, and the hardest to implement

due to required initial boundary conditions. With high degrees of freedom though FEM is the most accurate of the three methods, and is more suitable to multi-physics problems.

FVM similarly to FEM creates a mesh of polyhedral control volumes referred to as cells. Development of FVM was based on the laws of conservation, and as such only the energy fluxes entering and leaving a cell are calculated. This simplified approach reduces the computational load making CFD analysis of fluids more efficient. FVM has been shown to be accurate as FDM and low-order degrees of freedom FEM analysis (Blazek 2001).

3.2.1 Finite Volume Method

In the first process of FVM the partial derivative equations are integrated over each of the individual cells that the domain has been split into. After this the Gauss theorem is used to convert the volume integrals of the convection and diffusion terms into surface integrals. The resultant integrals are transformed into discrete ones and evaluated numerically, represented by the example taken from (Moukalled, Mangani & Darwish 2016) shown below:

$$\underbrace{\frac{\partial(\rho\phi)}{\partial t}}_{\text{transient term}} + \underbrace{\nabla \cdot (\rho\mathbf{v}\phi)}_{\text{convective term}} = \underbrace{\nabla \cdot (\Gamma^\phi \nabla \phi)}_{\text{diffusion term}} + \underbrace{Q^\phi}_{\text{source term}} \quad (3.1)$$

By dropping the front transient term we have the steady state form of the equation

$$\nabla \cdot (\rho\mathbf{v}\phi) = \nabla \cdot (\Gamma^\phi \nabla \phi) + Q^\phi \quad (3.2)$$

Considering the cell C in figure 3.2 and integrating the above equation over the cell the equation is transformed to

$$\int_{V_C} \nabla \cdot (\rho\mathbf{v}\phi) dV = \int_{V_C} \nabla \cdot (\Gamma^\phi \nabla \phi) dV + \int_{V_C} Q^\phi dV \quad (3.3)$$

By utilising the divergence theorem the volume integrals are replaced with surface integrals resulting in the equation form

$$\oint_{\partial V_C} (\rho \mathbf{v} \phi) \cdot d\mathbf{S} = \oint_{\partial V_C} (\Gamma^\phi \nabla \phi) \cdot d\mathbf{S} + \int_{V_C} Q^\phi dV \quad (3.4)$$

with **bold** characters representing vectors, Q^ϕ the source term, \mathbf{S} the surface vector, ϕ the conserved quantity, $\oint_{\partial V_C}$ the surface integral over the volume of the element C.

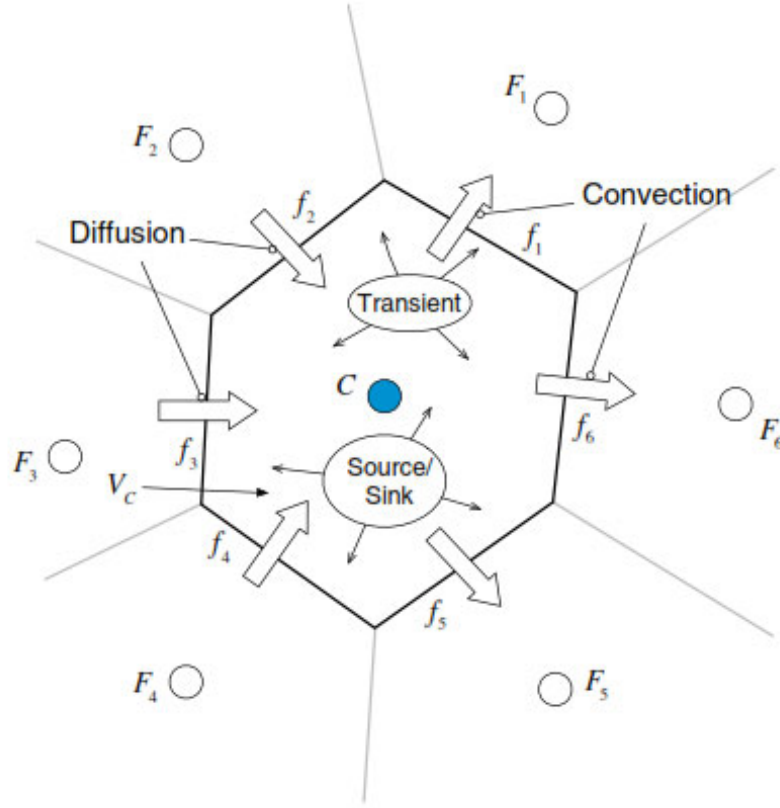


Figure 3.2: Conservation in a discrete element adapted from (Moukalled et al. 2016).

For the element C, the diffusion and convection fluxes, $\mathbf{J}^{\phi,D}$ and $\mathbf{J}^{\phi,C}$, are expressed by

$$\mathbf{J}^{\phi,C} = \rho \mathbf{v} \phi \quad (3.5)$$

$$\mathbf{J}^{\phi,D} = -\Gamma^\phi \nabla \phi \quad (3.6)$$

Equating a total flux sum of the convection and diffusion fluxes can be written as

$$\mathbf{J}^\phi = \mathbf{J}^{\phi,C} + \mathbf{J}^{\phi,D} \quad (3.7)$$

Using these identities, and replacing the surface integrals by the summation of fluxes over the faces of the element shown in 3.2, the surface integrals are transformed in to

$$\begin{aligned}
\oint_{\partial V_C} \mathbf{J}^{\phi,C} \cdot d\mathbf{S} &= \sum_{f \sim \text{faces}(V_C)} \left(\int_f (\rho \mathbf{v} \phi) \cdot d\mathbf{S} \right) \\
\oint_{\partial V_C} \mathbf{J}^{\phi,D} \cdot d\mathbf{S} &= \sum_{f \sim \text{faces}(V_C)} \left(\int_f (\Gamma^\phi \nabla \phi) \cdot d\mathbf{S} \right) \\
\oint_{\partial V_C} \mathbf{J}^\phi \cdot d\mathbf{S} &= \sum_{f \sim \text{faces}(V_C)} \left(\int_f \mathbf{J}_f^\phi \cdot d\mathbf{S} \right)
\end{aligned} \tag{3.8}$$

There is a major significance of this transformation on the properties of the FVM. As the governing equations have been transformed into a system of fluxes, where the flux leaving an element is the same as the flux entering the neighbouring element, this method is therefore conservative. Continuing on with the process of discretisation, we must do two things - evaluate the surface integrals at each face of the element and evaluate the volume integral of the source term. An n -point Gaussian quadrature rule yields exact results for polynomials of degree $2n - 1$ or less when approximating the definite integral of a function. Applying the rule here, the integral at a face f becomes

$$\int_f \mathbf{J}^\phi \cdot d\mathbf{S} = \int_f (\mathbf{J}^\phi \cdot \mathbf{n}) dS = \sum_{ip \sim ip(f)} (\mathbf{J}^\phi \cdot \mathbf{n})_{ip} \omega_{ip} S_f \tag{3.9}$$

Where ip and $ip(f)$ are an integration point, and number of integration points respectively. It can be seen that the more integration points there are, the higher the computational costs are for resolving the equations.

3.3 Turbulence Models

The simulation of turbulent flows is the significantly more difficult than laminar or inviscid flows (Blazek 2001, Cengel & Cimbala 2014). This is because turbulent flows are unsteady over time. They are chaotic and random flows swirling, vortical structures known as turbulent eddies, and flow instabilities (Solmaz 2023). There are a number of solver methods that have different levels of solution accuracy traded off for a reduction in compute power required as seen on figure 3.3

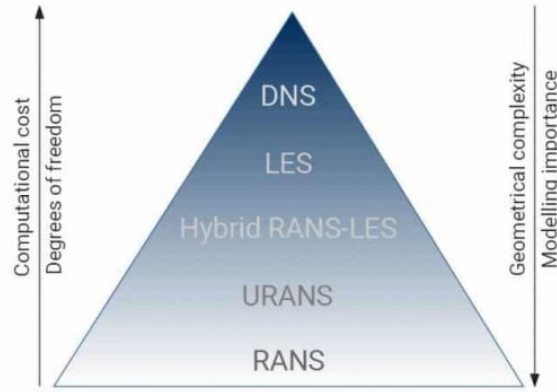


Figure 3.3: Hierarchy of turbulence solver methods (Simulations 2020).

The most accurate method of solving turbulence models is done by directly solving the time dependent Navier-Stokes equations, a process that is known as Direct Numerical Simulation (DNS). Considering that the minimum number of grid points for sufficient resolution is $Re^{9/4}$, and the required compute time is proportional to Re^3 (Blazek 2001), it is apparent that DNS is only a valid method for simple simulations of low Reynolds number. As such it is predominantly used in academia and the testing the accuracy of new turbulence models in development.

For industrial applications of CFD less CPU intensive methods of solving turbulence models are required. Large Eddy Simulations (LES), originally proposed by Smagorinsky in 1963 (Zhiyin 2015), is one such method. LES is the first level of accuracy lower than DNS and requires significantly less compute power while still providing analysis sufficient for complex engineering design and analysis purposes. In order to reduce the complexity of solving the full scale of flow, LES only resolves the large scale eddies and approximates the smaller eddies using simpler sub grid scale (SGS) models (Blazek 2001). This method retains a high level of accuracy as the large eddies contain most of the turbulent kinetic energy in a flow, approximately 80%, and are the main drivers of the diffusive process (Rodriguez 2019). Conversely the small scale eddies are much more homogeneous and isotropic in nature, and thus more suitable for modelling.

Reynolds Averaged Navier-Stokes equations (RANS) is again another order of accuracy lower than LES, but requires far less CPU time, and also compliant with coarser grids compared to LES (Blazek 2001, Motsamai, Muiruri & Ndeda 2019). RANS method

doesn't directly resolve any of the eddies, and instead mathematically models all of the mixing and diffusion in turbulent flows. The Navier-Stokes equations are time averaged with additional terms in the momentum equations called Reynolds stress tensors, and a turbulent heat flux vector. These terms account for turbulent momentum fluctuations, and the diffusive heat flux in the energy equation (2.4) respectively. Although not as accurate as LES, RANS still provides modelling that is accurate enough for engineering purposes and is by far the most used method in industrial applications.

Figure 3.4 shows the results of using these three main turbulence models on the same turbulent jet flow.

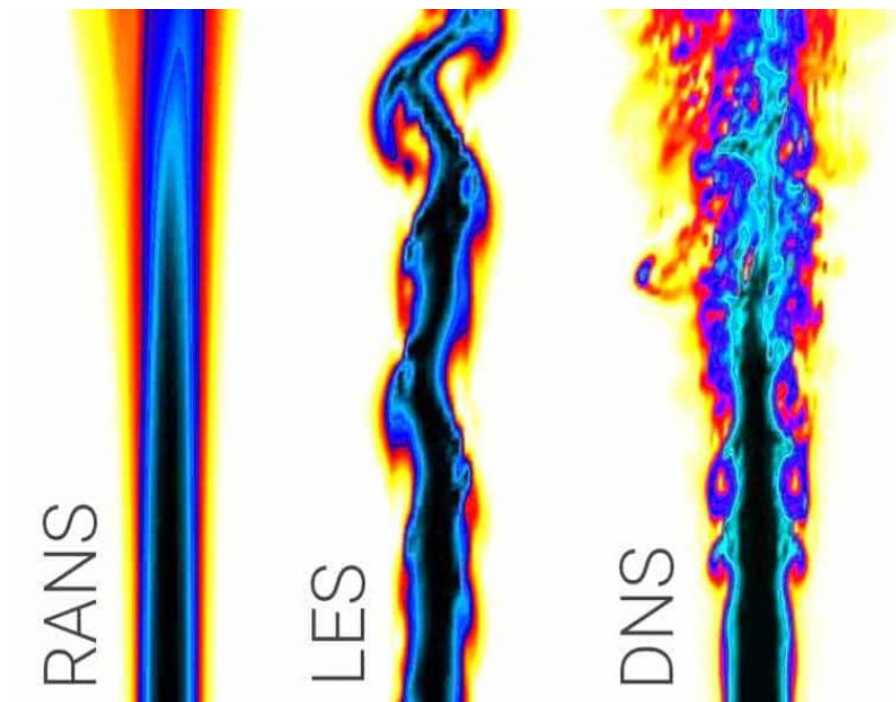


Figure 3.4: Comparison of results from RANS, LES, and DNS of a turbulent flow adopted from (Simulations 2020).

3.3.1 Reynolds Averaged Navier-Stokes

For RANS equation models to be a practical solution for CFD analysis they need to meet certain criteria (Malalasekera & Versteeg 2007). This include the model being able to:

- Be applicable to a wide range of problems
- Produce sufficiently accurate results

- Be simple and economical to run

There are a number of RANS models in the literature and available for use in CFD software applications. Typically they are categorised by the number of transport equations that need to be solved (Malalasekera & Versteeg 2007).

Table 3.1: RANS models categorised by their number of equations.

No. of transport equations	Name
Zero	Mixing-length model
One	Spalart-Allmaras model
Two	k- ϵ model
	k- ω model
Seven	Algebraic stress model
	Reynolds stress model

The seven equation Reynolds stress model has a considerable uptake in processing power to complete. As such, two of the most commonly used RANS models in industry are the k- ϵ and the k- ω models. The k (turbulent kinetic energy) - ϵ (rate of dissipation of turbulent kinetic energy) and the k - ω (specific rate of dissipation of kinetic energy) are very similar (Frei 2017). K- ϵ modelling applies a wall function to the flow, which simplifies the computation and increases the convergence rate. This makes the model useful in applications where the area of interest is the fluid flow. Due to the use of the wall function however makes the k- ϵ method less applicable to the forces of a fluid flow acting on an object as the buffer region is not simulated.

By comparison the k- ω resolves the boundary layer to a much higher level of accuracy as the model does not use a wall function. A downfall of the model is it's sensitivity to the ω values beyond the boundary layers in free shear flows (Asako, Japar, Mohamed, Sidik & Yusof 2020). The k- ω model is also harder to converge as it less linear than the k- ϵ , and also requires more accurate initial conditions of the flow (Frei 2017). Studies such as those done by Motsamai et al. (2019) have shown that the k- ω model is more accurate to experimental data when investigating the forces a flow exhibits on an object.

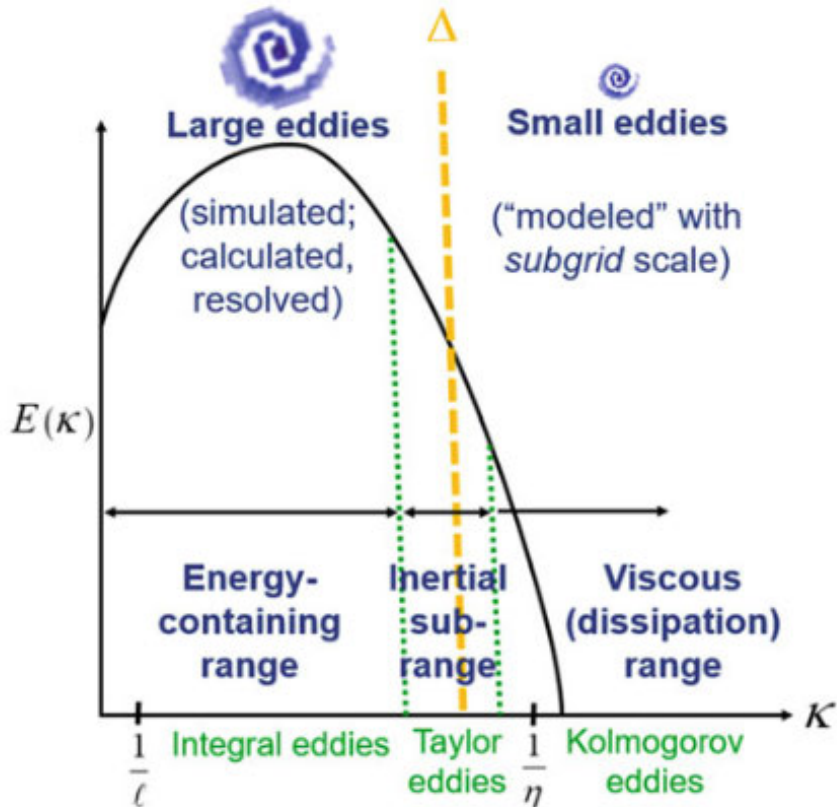
ANSYS Fluent has a sub variant of the k- ω method, the Shear-Stress Transport (SST) k- ω method. This type of model aims to improve the standard k- ω by gradually changing from the standard k- ω in the boundary layer to the k- ϵ method at the outer regions of the boundary layer (Ansys 2011). By taking this approach the integration of the model

into the boundary layer and the free shear flows allows good accuracy in both a fluids flow characteristics and the forces the fluid flow exhibits on a body.

3.3.2 Large Eddy Simulations

The original paper which formed the basis for this project utilised the LES method, so it is important to understand the method and differences to RANS. As mentioned in the Turbulence Model Chapter 3.3, LES reduces the compute time by filtering eddies by their size Δ , to determine if they are resolved directly or estimated using SGS models. The most common cut-off eddie size in three dimensional simulations is taken as the cube root of the grid cell volume. There is no gain in accuracy from selecting a cut-off size smaller than the grid size as the finer flow details are lost anyway (Malalasekera & Versteeg 2007). The spatial filtering of eddies can be visualised as seen in figure 3.5

Figure 3.5: LES size filtering of eddies adopted from (Rodriguez 2019).



Spatial filtering of the Navier-Stokes equations is achieved through the application of a filter function $G(\mathbf{x}, \mathbf{x}', \Delta)$ (Pomraning 2000).

$$\overline{u_i}(\mathbf{x}) = \int_V G(\mathbf{x}, \mathbf{y}) u_i(\mathbf{y}) d\mathbf{y} \quad (3.10)$$

The filter function $G(x,y)$ must fulfil the condition

$$\int_V G(\mathbf{x}, \mathbf{y}) d\mathbf{y} = 1 \quad (3.11)$$

Note the over-bar in (3.10) signifies spatial filtering, and not to be confused with time-averaging as it is usually used to indicate in RANS equations. The most commonly used filter functions are the box, Gaussian, triangle, and spectral cut-off filters (Pomraning 2000). The box filter equation:

$$G(x, y) = \begin{cases} 0. & \|x - y\| > \Delta(x)/2 \\ 1/V(x) & \|x - y\| \leq \Delta(x)/2 \end{cases}, \quad (3.12)$$

The Gaussian filter equation:

$$G(\mathbf{x}, \mathbf{y}) = \left(\frac{A}{\pi}\right)^{1/2} \exp(-A(\mathbf{y} - \mathbf{x})^2) \quad (3.13)$$

The Triangle filter equation:

$$\frac{\Delta^2(\mathbf{x})}{4} G(\mathbf{x}, \mathbf{y}) = \begin{cases} 0. & \|\mathbf{x} - \mathbf{y}\| > \Delta(\mathbf{x})/2 \\ \Delta(\mathbf{x})/2 - \|\mathbf{x} - \mathbf{y}\| & \|\mathbf{x} - \mathbf{y}\| \leq \Delta(\mathbf{x})/2 \end{cases}, \quad (3.14)$$

The reason for the existence of multiple filter equations is because no one filter is generally applicable to all simulations. Filters can be considered to have smooth, semi-sharp, or sharp cut-off, and will output different solutions for the SGS model. Smooth filters, such as the Gaussian, tend to blend the edges of the large and small eddy cut off boundary. Smooth filters can over dissipate the large eddy turbulent energy to the SGS. Sharp filters by contrast are much more binary in nature, and the boundary between large and small eddies is clearly defined. The volume-averaged box filter has a sharp cut-off, which calculates the transfer of energy from the large scale to small scale eddies much better. However convergence issues may occur with too small a value of Δ - as $\Delta \rightarrow 0$, the LES \rightarrow

DNS (Zhiyin 2015). The spectral filter is sharp, but less so than the box filter. Finally the triangle filter, based on the Gaussian filter, is smooth but with better contrast between the large and small scale eddies.

Due to extensive research and applications in the last 30 years there are a number of SGS models, some of the more common models as listed by Rodriguez (2019) include:

- Standard Smagorinsky model
- Dynamic Smagorinsky model
- Localised dynamic model
- Wall-adapting local eddy-viscosity (WALE) model
- Dynamic global-coefficient model
- RNG-LES model
- Kinetic energy subgrid-scale model
- σ -SGS model

SGS model types can have significant impacts on the results of a LES. Selection of the correct SGS model should be based on the flow characteristics, model suitability, and literature review or industry practice. LES simulations must be verified against either of experimental data, a DNS model, or other verified simulation data. ANSYS recommends for LES starting with the WALE or Dynamic Smagorinsky model (Gerasimov 2016).

3.4 Meshing Quality

The manner in which a domain is discretised into a mesh of cells has a pronounced effect on the accuracy and stability of the numerical simulation (Ansys 2010). As Knupp (2007) described, *Mesh quality concerns the characteristics of a mesh that permit a particular numerical PDE simulation to be efficiently performed, with fidelity to the underlying physics, and with the accuracy required for the problem.* Mesh quality can be assessed through geometric parameters of the cells, such as aspect ratio, Jacobian, orthogonal

quality, skewness, and squish to mention a few. The distribution of cells is also an important aspect of mesh quality. In critical areas of the domain, such as boundary layers, mixing zones, phase interactions etc in these areas the mesh needs to be more refined to produce accurate simulation results. To reduce compute times, in non critical areas where the flow is more likely to be laminar the mesh can be more coarse. Mesh quality however, goes beyond geometric metrics of the cells. When assessing mesh quality the solver type, the solution, and the desired output need to be taken into consideration also (Diskin & Thomas 2012, Knupp 2007). The mesh can effect the time taken for iterative solvers to reach convergence, or even prevent them from reaching convergence (Knupp 2003).

Diskin & Thomas (2012) investigated the effects of mesh irregularities on the finite-volume method for 2D models. They found that gradient, truncation, and discretisation errors were affected by mesh quality to vary degrees. Truncation errors in particular were extremely sensitive to mesh regularity. Gradient errors were proportional to the aspect ration, where the proportion varied between mesh cell shapes and fit. Discretisation error sensitivity was similarly related to the cell shape with triangle cells being very insensitive, and mixed / quadratic cells being somewhat affected by mesh quality.

ANSYS Fluent allows the user to check a mesh prior to running a simulation. The mesh check evaluates the structure of the cells, firstly ensuring the cells have the correct number of faces and nodes for the designated shape. Face handedness and face node order is checked, then element type consistency. Fluent finally checks the quantities of the cells, faces, and nodes as compared to the mesh file (Ansys 2010). Fluent also has an operation that iteratively improves the mesh quality towards a target quality value.

3.5 Initial and Boundary Conditions

In order for a CFD simulation to produce accurate results, the initial and boundary conditions must be correctly defined (Blazek 2001, Rodriguez 2019). These conditions also affect the stability and convergence rate of the simulation. Initial and boundary conditions in CFD represent the mathematical equations describing how the walls of the domain interact with the flows, and the characteristics of how the flow enters the domain. ANSYS Fluent has a broad range of boundary and initial conditions, however, for brevity, only the conditions pertinent to this research project will be discussed.

The no-slip condition is based on the discovery by Ludwig Prandtl in the early 1900s (NASA 2021a). In viscous flows past an object, at the surface of the object the velocity of the fluid is effectively zero with molecules sticking to the surface. Layers of fluid increasing in velocity form on top of one another away from the surface until the fluid is flowing at its characteristic velocity. The height of this boundary layer is dependent on the Reynolds number of the fluid.

Periodic boundaries allow for the simplification of repetitive geometries and flow patterns in a model. This makes them well suited for LES and DNS applications due to the reduction in compute time (Rodriguez 2019). Two faces of the domain or object are selected for the model to be treated as if the faces were connected. This allows the simulation to let flows and fluxes enter or exit from one face and re-enter or exit from the other face. A real world infinite domain maybe approximated into a smaller domain in a CFD model using the periodic boundary (SimScale 2022). In ANSYS Fluent establishing a direct periodic boundary condition requires that the two faces have the same number of elements. Alternatively a non-conformal periodic boundary condition can be created for unstructured meshes, however this is not as ideal.

For multiphase flow using the volume of fluids method, there are limited inlet conditions available in ANSYS Fluent. Pressure inlets allow the user to select the secondary phase for the inlet, flow specification method, free surface level, bottom level, and velocity magnitude (Rodriguez 2019). Pressure inlets are suitable for both compressible and incompressible fluids entering a domain. Pressure outlets allow the fluids to leave the domain. By setting a pressure outlet to zero gauge pressure, fluids leave the domain as driven by flow determines and does not impart any extra forces on the flow. This is particularly useful in re-creating open atmospheres. Pressure outlets in multiphase flow permit the user to specify the gauge pressure at the outlet, the free surface level, and the bottom level.

3.6 Volume of Fluids

The Volume of Fluids (VOF) method is a numerical technique used in CFD in order to simulate the behaviour of multiple immiscible fluids in a shared computational domain. This method is valuable in particular for studying complex fluid-fluid interactions and

capturing free-surface flows such as required for this research project. It provides a detailed representation of fluid interfaces, making it useful in a wide range of applications, including aerospace, automotive, and environmental engineering (Katopodes 2018).

In the VOF method, a volume fraction field is defined within the computational domain for each individual cell. This field assigns a value between 0 and 1 to each grid cell, indicating the ratio of that cell occupied by a primary and secondary fluid (Al-Salami, Kamra & Hu 2021). The interface between two immiscible fluids is not explicitly tracked but is implicitly represented by the sharp change in the volume fraction value. The VOF method key advantage is its ability to maintain the sharpness of fluid interfaces, and rapid deformation.

To simulate fluid flow using the VOF method, the governing Navier-Stokes equation are solved alongside a transport equation for the volume fraction field. In a transient solver process, this transport equation tracks how the volume fraction changes over time due to advection and diffusion. When the volume fraction reaches a certain threshold, typically 0.5, the cell is considered to be either primary or secondary fluid depending on the value. This approach makes the VOF method particularly suitable for simulating dynamic and complex flows where the interface moves and deforms like splashing, breaking waves, or bubble formation.

3.7 Validation of CFD Modelling

Validating a CFD simulation model is a crucial step to ensure that it accurately represents real-world fluid flow phenomena. The process usually involves comparing CFD results with experimental or benchmark data. It is commonly known as a requirement in the field of CFD in order to produce results of meaning. As described by a variety of texts such as Cengel & Cimbala (2014), Malalasekera & Versteeg (2007), and OBERKAMPF & TRUCANO (2002) , to produce an accurate CFD model typically follows most or all of these key steps:

- **Define Objectives and Metrics:** Begin by clearly defining the objectives of the simulation and the specific metrics you intend to validate. What aspects of the flow are you interested in? Common metrics include velocity profiles, pressure distributions,

and turbulence characteristics.

- **Collect Experimental Data:** Acquire high-quality experimental data through physical experiments or from reliable literature sources. This data will serve as the reference for comparison with your CFD results.
- **Set Up the CFD Model:** Create a well-structured CFD model, ensuring it replicates the physical geometry and boundary conditions accurately. Use a grid resolution that is sufficient to capture the flow features of interest.
- **Run the Simulation:** Execute the CFD simulation, making sure to employ appropriate turbulence models and numerical schemes. Perform sensitivity studies on parameters like mesh size, time step, and turbulence model to assess their impact on results.
- **Post-Processing and Data Analysis:** Analyze the CFD results by extracting relevant data at the same locations and under similar conditions as the experimental data. Calculate error metrics such as root mean square error (RMSE) or relative error to quantify the discrepancies between simulation and experimental results.
- **Compare and Interpret Results:** Compare the CFD data to the experimental data and interpret the differences. Carefully consider the magnitude and location of discrepancies, as well as trends in the data. Small differences might be acceptable, but large disparities require investigation.
- **Refine the Model:** If significant discrepancies exist, make appropriate adjustments to the CFD model. This may involve refining the mesh, using a different turbulence model, or reassessing boundary conditions.
- **Reiterate and Document:** Repeat the simulation and validation process iteratively, making incremental improvements to the model until a satisfactory level of agreement is achieved between CFD results and experimental data. Document each iteration and the rationale behind changes.
- **Report and Communicate:** Present the validated CFD results along with a comprehensive report detailing the methodology, assumptions, and validation process. Communicate the limitations of the model and uncertainties in the results.
- **Peer Review:** Seek peer review or expert consultation to ensure that your validation process is rigorous and unbiased.

Validation is an ongoing process, and it's essential to continuously assess the accuracy and reliability of a CFD model, particularly when applied to new scenarios or conditions.

3.8 Coherent Structures

Turbulence which is often thought of as fully random flows, has been shown to have quasi-deterministic large-scale structures in the free shear flow. Hussain (1986) describes coherent structures as *a connected turbulent fluid mass with instantaneously phase-correlated vorticity over its spatial extent*. As coherent structures are implicit in nature, the exact definition is not defined and is left somewhat in the abstract. Whilst observing a vortex is easily achieved, determining how far out from the centre of the rotation the edge of the vortex extends is open to interpretation and debate (Altimemy, Attiya, Daskiran, Liu & Oztekin 2018). Figure 3.6 shows a diagram of a coherent vortex structure formed in a water flow over a backward facing step. Coherent vortical structures are responsible for a large portion of the transport of heat, mass, and momentum in a fluid flow. By comparison the smaller eddies are responsible for the diffusion of fluxes.

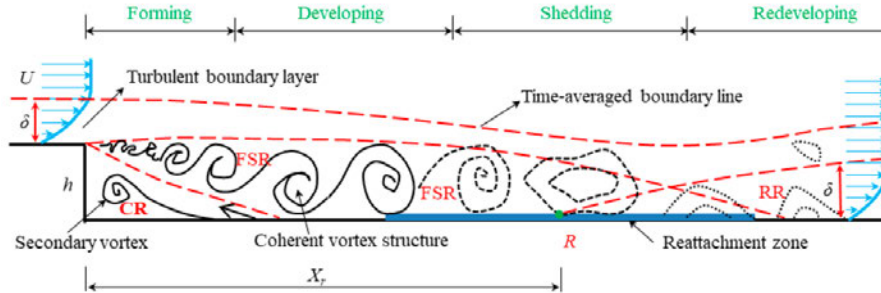


Figure 3.6: Coherent structures formed in fluid flow over a backward facing step adapted from (Wang et al. 2019).

When identifying a coherent structure a criterion threshold is determined and if the physical properties meet the threshold than the structure is determined to be coherent. Physical properties under consideration are the normalised vorticity and or strain. Vorticity in a mathematical model can be identified through the use of instantaneous velocity-gradient tensors (GREEN, Rowley & Haller 2007). The tensors can be decomposed into the symmetric S (strain) and anti-symmetric Ω (rotation) components. This method of vortex identification is known as Eulerian method.

An alternative method, the Lagrangian method, considers the trajectories of fluid par-

ticles. The advantage of using Lagrangian Coherent Structures (LCS) is that they are independent with respect to rotation of the reference frame (GREEN et al. 2007). Altimemy et al. (2018) showed in their study that structures that weren't detected by the Eulerian method were shown by using LCS when compared the two methods. They also showed a much higher level of resolution of the structures in the flow field. LCS is much more computationally demanding than the Eulerian method. Sub methods of LCS are currently being explored to reduce the demands of the process, as discussed by Peacock & Dabiri (2010).

3.9 Chapter Summary

This chapter has presented the information that was required to be researched in order to complete the project. The original intent for the research project was to utilise the LES turbulence model for a direct comparison between Attiya et al. (2019) results using OpenFOAM and the results obtained using ANSYS Fluent. Through the literature review, it soon became quickly apparent that the compute times for a LES model would be too time consuming and impractical for the purposes of this research project. In order to achieve the aims of this project in the time frame given, it was decided to utilise the RANS model instead.

Chapter 4

Model Validation

4.1 Chapter Overview

The methods used to validate the ANSYS simulations are discussed in this chapter. It includes a review of a previous case study utilising OpenFOAM, a description of the analogous simulation setup in ANSYS Fluent, and a discussion of the ANSYS simulation results. The chapter ends with brief statement concluding the findings of the model validation.

4.2 Previous Works

Attiya et al. (2019) analysed multiphase flows over a series of different finite plate geometries in order to characterise the resultant turbulent flow structures and hydrodynamic loads on the plates. In their study the software package used was OpenFOAM, and it's interFoam VOF solver which uses a Multi-dimensional Universal Limiter for Explicit Solutions (MULES). The Pressure-Implicit with Splitting of Operators (PISO) algorithm was specified for the transient solver pressure-velocity coupling, an adjustable time step based on Courant number, second order time discretisation were the model parameters used in the simulation. The model geometry was broken into subdomains with a nested structured mesh with non-conformal interfaces. Mesh at the critical finite plate and free surface areas was refined with a gradual increase in cell size with the increase in distance from the plate and free surface. The simulation geometry and input parameters are shown

in figure 4.1 and table 4.1. The aspect ratio of the plate is the ratio of it's length to height.

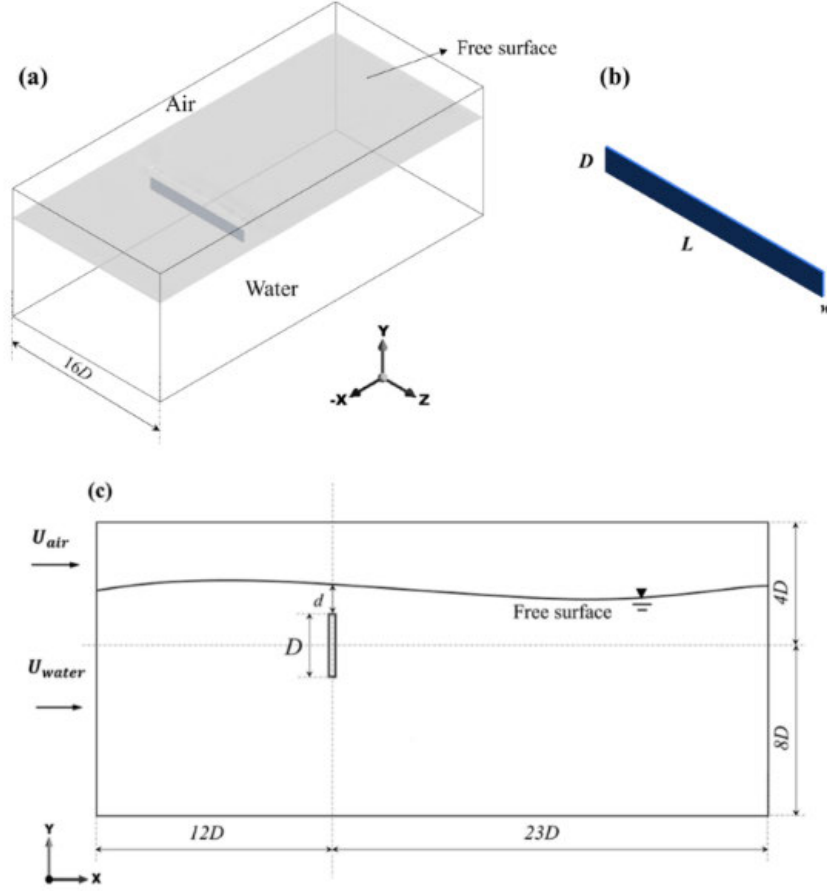


Figure 4.1: Diagram of the computational domain, plate geometry, and side view of the OpenFOAM simulation adapted from (Attiya et al. 2019).

The study found that the aspect ratio of the plate affected vorticity in the fluid and the hydrodynamic loads. For aspect ratios of 5 and 10 there was significant vorticity generation in the flow upstream of the plate, however for the aspect ratio of 2.5 there was no significant impact on vorticity upstream. Each increase in aspect ratio saw the location of the hydraulic jump moved close to the plate location, and an increase in upstream turbulence. The Attiya et al. (2019) proposed that it was this increase in upstream turbulence which was the cause of the reduction in the co-efficient of drag and lift values of the plate as the aspect ratio increased. The full set of drag results of this study can be found in Appendix D.

Table 4.1: Input parameters used in OpenFOAM LES simulation adopted from (Attiya et al. 2019).

Parameter-Value-Unit					
w	0.01	[m]	ρ_w	998.2	[kg/m ³]
D	0.1	[m]	ρ_{air}	1.225	[kg/m ³]
L	0.25, 0.5, 1	[m]	Re_w	50,000	[-]
d	0.015	[m]	U_{water}	0.5	[m/s]
Fr	1.30	[-]	U_{air}	0.01	[m/s]

4.3 Validation Simulation Setup

Attiya et al. (2019) described using a fully structured mesh of three varying mesh densities for their mesh sensitivity test. A coarse mesh N1, was reported as having 3×10^6 cells, a semi refined mesh N2, 7×10^6 cells, and a fine mesh N3, 14×10^6 cells. The nested mesh grids were also described with N1 being a 363, 156, 226 grid, N2 being a 408, 186, 326 grid, and N3 being a 526, 236, 424. Cell sizes were also described with the cell sizes at the plate varying between 0.8, 0.5, and 0.3mm for the coarse, mid, and fine meshes, and a global maximum size of 3mm for all three meshes. Refinement of the mesh at the plate was achieved with a mesh bias factor of 4 towards the plate.

Upon attempting to re-construct the domain for a validation simulation it was soon discovered that the reported number of cells did not align with the mesh grids or cell sizes. The nested coarse mesh grid of 363, 156, 226 would result in 12.8×10^6 with the remaining outer mesh still to be modelled. Similarly, if the entire domain of the smallest plate ($0.825\text{m} \times 1.2\text{m} \times 3.5\text{m}$) was divided into the largest cell size reported of 3mm, this would result in 128×10^6 cells.

In an attempt to continue with the validation, the domain was re-created with a fully structured hex mesh of 12.2×10^6 cells. A bias factor of 4 towards the plate was applied, and the cells directly perpendicular to the plate surfaces were of 1.5mm edge size. Figures 4.2 and 4.3 show the structured mesh and it's bias refinement to the plate.

This created a mesh of decent quality, virtually all cells had a Jacobian quality of 0.999, and skewness 0.02. Aspect ratio was 1.89 for more than half the cells, and only approx five percent of cells over 10 but less than 18. Average cell quality was 0.60 with 1.05 percent of cells being of quality less than 0.2. Lower cell quality and aspect ratio occurred due

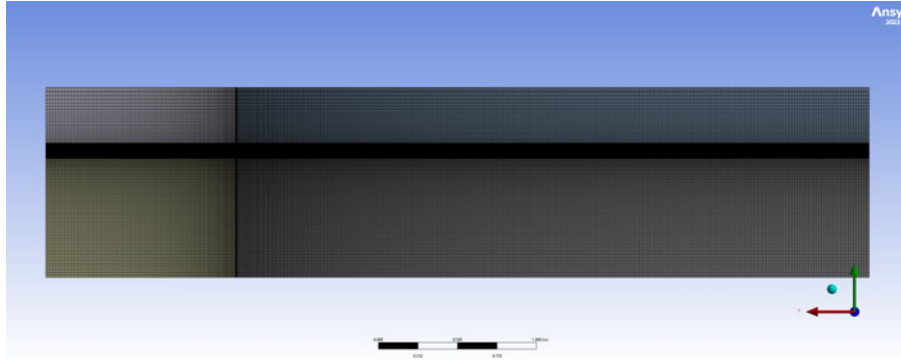


Figure 4.2: An overall view of the mesh used for validation

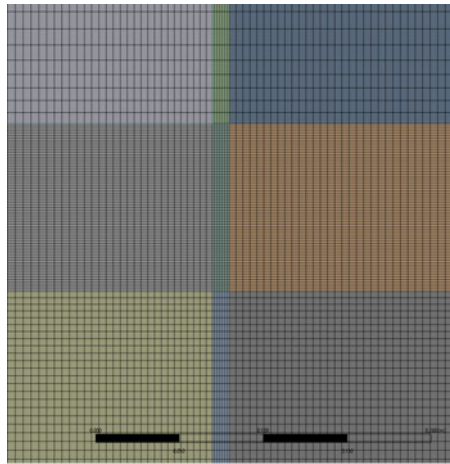


Figure 4.3: A close up of the mesh refinement at the plate

to the mesh bias creating elongated cells at the furthest points away from the plate. These were improved with Fluent improve mesh operation until quality was over 0.2.

Boundary conditions for the validation model were as follows:

- Pressure inlet with 0.5m.s^{-1} air and liquid fluid velocity
- Periodic translational boundary on the side walls of the domain
- No-slip wall to generate the boundary layer on the bottom of the domain and the surfaces of the plate
- Zero gauge pressure outlet on the top of the domain to simulate the atmosphere
- Zero gauge pressure outlet at the end of the domain to allow the fluids to freely exit the domain

Solver settings used for the simulation were:

- Steady State Solution
- Multiphase enabled with implicit body force, constant water tension 0.072
- Pressure-velocity Coupling Scheme - SIMPLE
- Spatial Discretisation; Gradient - Least Squares Cell Based, Pressure - PRESTO!, Momentum - Second Order Upwind, Volume Fraction - Compressive, Turbulent Kinetic Energy - Second Order Upwind, Specific Dissipation Rate - Second Order Upwind
- Under-relaxation factors reduced by 25 percent for solution stability
- Solution Initialisation - Standard, computed from inlet, Flat open channel initialisation method.

4.4 Validation Results

The validation simulation converged after 2342 iterations. Drag force experienced by the plate was 4.342N which correlates to a coefficient of drag of 1.392. Lift force acting on the plate was 2.4505N which correlates to a coefficient of lift of 0.7861. Comparing these results to those of Attiya et al. (2019) in table 4.2, the coefficient of drag was significantly lower, the coefficient of lift significantly higher, and the average $Y+$ value massively higher.

Table 4.2: Comparison of results from the validation simulation.

	C_d	C_l	$Y+$
Bashar LES Model	1.789	0.813	1.814
Validation RANS Model	1.392	1.403	32.030
Variation Percentage	-22.178	72.613	1666.101

There was significant variation from the two sets of results, a variation of less than 10% would be required to consider the model loosely validated and less than 5% ideally. In an attempt to validate the model again the mesh was refined to cell sizes comparable with Attiya et al. (2019). The cell size on the plate was reduced to 1mm, and the largest global cell size was reduced to 3mm. This resulted in a very fine mesh consisting to 77 million cells. The HPC ran the solver on 52 cores, and completed 25, 000 iterations over approximately 6 days without converging. Drag force was hovering around the 4.3 to

4.4N of force which correlates to a coefficient of drag of 1.38-1.41. Considering the coarser mesh converged with a coefficient of drag of 1.39, it was apparent that mesh refinement would not bring the results into alignment for validation, and that the compute times for completing simulations of that cell density are impractical.

4.5 Chapter Summary

The results of the validation simulation were not to a level of agreement with Attiya et al. (2019) results in order to consider the ANSYS model validated. Contributing factors to the significant difference of results would be:

- Inherent differences between LES and RANS models
- Discrepancies in the reported mesh of Attiya et al. (2019) model resulting in a large y^+ value of ANSYS model
- Potential differences in boundary conditions

Based on this the aims of this research project were modified. Attempting a direct comparison between new plate geometries with the results from the previous works is no longer feasible. This project will now aim to re-model the original plate geometries, as well the new curved geometries and compare the results.

Chapter 5

Domain Size and Mesh Sensitivity

5.1 Chapter Overview

This chapter describes the models domain size sensitivity and mesh sensitivity testing. This process ensures that the results of the simulation aren't being affected by either the size of the domain or the refinement of the mesh. Results shown here were obtained using the 250 wide flat plate, with full polyhedral mesh with BOI refinement.

5.2 Domain Size Testing

In order to ensure that the domain size was allowing full development of the flow characteristics without inhibiting the result, the domain size was tested. Using the original paper of (Attiya et al. 2019) as a guide, the domain was initially given a base design approximately the same as the reference material size. First the simulation was run with the base size and the results of the simulation recorded. Then the distance from the edges of the plates to the walls of the domain was increased before running and comparing the results of the two simulations. This process was repeated until the simulation result variation was less than five percent, it was assumed that the result was independent of the domain size. Similarly, once the wall distance was established, the process was repeated gradually increasing the distance from the plate to the outlet until there was a convergence of simulation results. In figure 5.1 the domain dimensions being varied are shown diagrammatically, with X1 being the wall gap distance, and X2 the outlet distance.

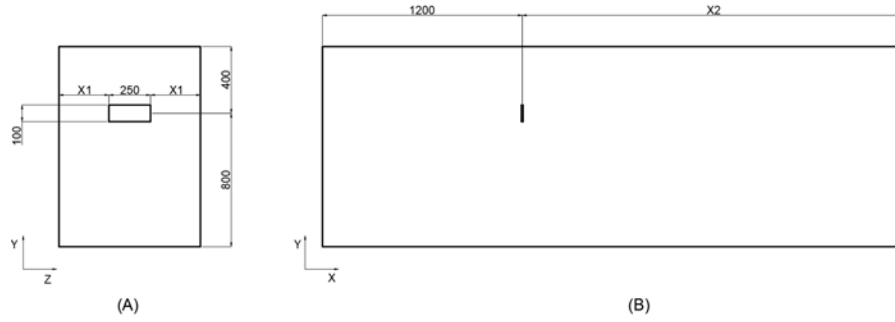


Figure 5.1: Domain size testing diagram. (A) width test, and (B) length test.

It can be seen in table 5.1 that the result variation was less than three percent between having a wall distance of 300mm and one of 400mm. Based on this it was determined that the result was independent of the domain width.

Table 5.1: Results of domain width test.

Wall Distance (mm)	Drag (N)	Lift (N)
300	4.1981	2.5053
400	4.1374	2.454
Difference %	-1.45	-2.05

While performing the outlet distance test there was very good agreement between the 2.5m and 3.5m outlet distance. By itself this would be a good indicator of result convergence, however during the simulation there was a large number of cell faces experiencing reverse flow at the outlet,. Reverse flow is a typical indicator that fluid is trying to re-enter the domain due to turbulence as a result of the domain not being long enough for turbulent dissipation in the model. Moving the outlet distance to 4.5m there was a significant jump in the drag force from the 3.5m result, a nearly seven percent difference in drag force. As shown in table 5.2 result variation between the 4.5m and 5.5m outlet distance was of less than three percent so the result was determined to be independent of domain length at 4.5m. At this length there was also relatively low number of cells faces experiencing reversed flow at the outlet.

Table 5.2: Results of domain length test.

Outlet Distance (m)	Drag (N)	Lift (N)	Drag Difference (%)	Lift Difference (%)
2.5	4.0335	2.5216		
3.5	3.9213	2.5218	-2.78	0.01
4.5	4.1909	2.4990	6.88	-0.90
5.5	4.0682	2.5383	-2.93	1.57

5.3 Mesh Sensitivity

Mesh refinement is a balancing act between the models accuracy and compute cost demands. The mesh needs to be sufficiently refined to fully define the current eddies, without being over refined and having needlessly long calculation times. The 250mm wide flat plate with a domain having 300mm wall distance and 4.5m outlet distance, as per the domain size testing, was used to perform the mesh sensitivity test. Five mesh sizing specifications were used to refine the mesh. An edge sizing on the plate, five layers of inflation on the plate with default settings, an inner wake BOI, an outer wake BOI, and a BOI centered on the free surface level. Wherever specified sizing methods overlap the smaller of the two conflicting methods takes priority. The BOI setup is displayed in 5.2.

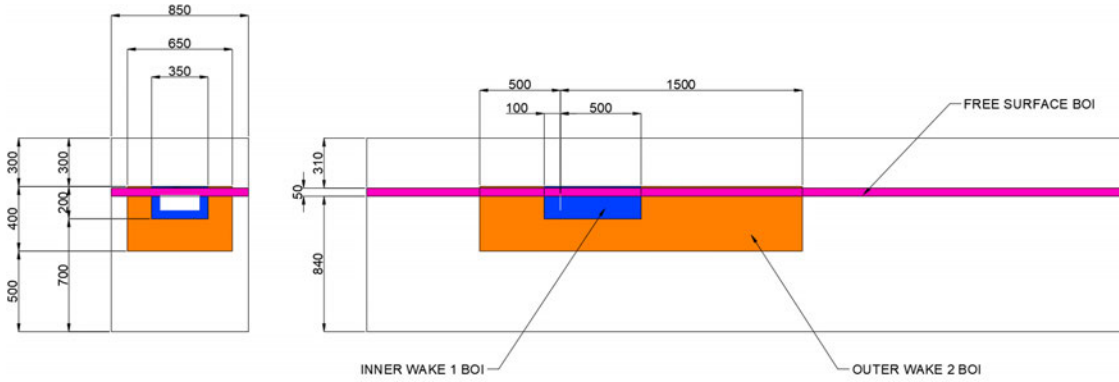


Figure 5.2: Domain size testing diagram. (A) width test, and (B) length test.

Results of the mesh sensitivity test are given in table 5.3. The difference in the drag force and lift force varies by 6.56 and 1.25% for the coarse and semi fine mesh densities of 13 and 19.4 million cells. The difference in the drag force and lift force varies by -0.47 and 2% for the semi fine and fine mesh densities of 19.4 and 41.4 million cells. Based on the latter result it was deemed that mesh independence was achieved with the cell sizings for the semi fine mesh. For the rest of the simulations these parameters for the plate edge size and wake 1, wake 2, and free surface BOI cell sizes.

Table 5.3: Results of mesh sensitivity test.

Mesh	Plate Edge (mm)	Wake 1 (mm)	Wake 2 (mm)	Free Surface (mm)	Global Max (mm)	Cells	Drag (N)	Lift (N)	Y+
Coarse	0.5	5	15	8	30	13x10 ⁶	3.9655	2.472	1.57455
Semi Fine	0.4	4	14	7	30	19.4x10 ⁶	4.2237	2.5014	1.20182
Fine	0.3	3	12	5	30	41.4x10 ⁶	4.2099	2.4548	1.00842

5.4 Chapter Summary

Establishing domain size and cell size independence was discussed in this chapter. It outlined the systematic process of increasing domain size, and refining mesh sizes until the simulation results were shown to be independent. The domain and cell sizes that reached independence will be used as constant parameters for the rest of the simulation completed for this project.

Chapter 6

CFD Simulation Setup

6.1 Chapter Overview

This chapter describes the setup of the models used for simulations run as part of the project. Information here includes the plate and domain geometry, meshing techniques of the domain, and the parameters of the solver used in ANSYS Fluent.

6.2 Plate and Domain Geometry

citelsmulti analysed flat plates of varying aspect ratios in their analysis. These were modelled as 10mm thick plates, of 100mm depth, and three widths of 250, 500, and 1000mm. In single phase flows there are known values for some basic shapes, a 2d flat plate has a C_d value of 1.98, and a semi-circle plate concave into the direction of the flow has a C_d value of 2.30. Based on this it was decided to test plates with a 180 degree curve in the plate and simulate this with the concave side facing into the flow. A 50mm radius was used for the outer face curve to maintain the same frontal area perpendicular to the flow. The profile of the plates is shown below in (A) of figure 6.1.

The process of domain sizing to ensure results were independent of domain size were discussed in Chapter 5. Based domain was a plain rectangular prism of fixed height, and depth in the y and x planes respectively, while the width of the prism varied to maintain a distance of 300mm to domain walls. The center of the plate radius was located at the

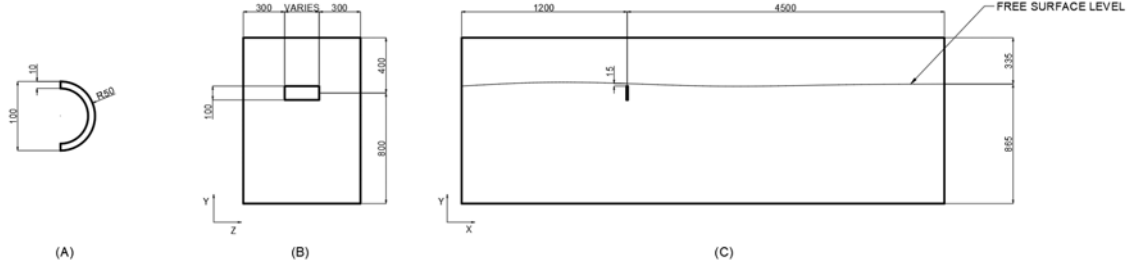


Figure 6.1: (A) Cross sectional profile of the curved plates, (B) YZ plane cross section of the domain, (C) YX plane cross section of the domain.

zero point of the co-ordinate system, the free surface was located 15mm above the top of the plate. The inlet was 1200mm upstream of the plate which allowed the flow enough space to develop any vortex shedding from the free surface, and the hydraulic jump to form. To allow the flow to approach a laminar state before exiting the domain, the outlet was required to be 4500mm from the plate. Figure 6.1 (B) and (C) shows the geometric setout of the domain.

6.3 Hex Dominant Mesh Steady Simulation

A fully structured hex mesh could not be created due to the curved side edges of the plate, so a multi-part hex dominant mesh was created for a close compromise. The domain was split into a multi-part body to allow for mesh refinement in critical areas, this also ensured that the nodal points between the parts were common.

An inner body was created with a boolean subtract plate entity inside a rectangular prism. The prism was offset 50mm from the extremities of the plate giving 350W x 200H x 150D prism. This body had a tetra mesh with a maximum cell size of 5mm and 1mm cell sizes applied to the faces of the plate. Inside the Fluent stage of the workbench workflow, the tetras were converted to polyhedral cells. Polyhedral cells were used because they typically perform the same or in some cases better than tetra cells, and solve slightly faster than tetras.

Volumes of the domain directly above, below, in front, and behind the plate volume were extended to the domain edges. The edges of these volumes were split into specific number of divisions, with a bias factor of 5 condensing the cells towards the plate. The number of divisions was selected to suit an average cell size of 6mm. The remaining volumes

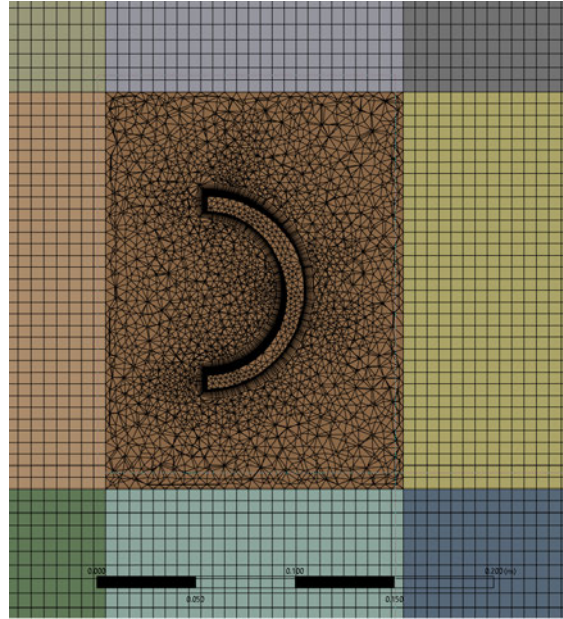


Figure 6.2: Cross sectional profile of the curved plate with hex dominant mesh.

were created with a edge sizing to suit the neighbouring bodies. A face sweep was used to create structured hex mesh throughout the domain as a whole, excluding the volume of tetras. A cross section through the curved plate showing the hex and tetra mesh is depicted in figure 6.2.

For the hex dominant mesh the same boundary conditions that were used for the model validation in Chapter 4 were used here. Wall Y plus is a non dimensional unit that indicates how well the boundary layer is being captured. A value of around one indicates that the boundary layer is being well captured, values of 1 to 5 indicate that the first cell node is in the laminar zone, and 5 to thirty is transitioning into the turbulent zone. After running the simulations for the original mesh design it was discovered that the Y^+ values were too high and that the mesh design needed to be revised and more refined around the edges of the plate. Inflation layers were thus added to the surface of the curved plate in order to capture the boundary layer correctly. 10 inflation layers were added with a growth rate of 1.1 and a smooth transition properties. The simulations were then re-run with the new mesh specification. The results in Chapter 7 show that there was mesh induced turbulence.

6.4 Hex Dominant Mesh Transient Simulation

In an attempt to eliminate the mesh induced turbulence the Hex Dominant Mesh was re-run with a transient solver. The domain, meshing, and boundary conditions were identical to the steady state model with the only variation being the solver setup. Solver settings used for the simulation were:

- Transient
- Multiphase enabled with implicit body force, constant water tension 0.072
- Pressure-velocity Coupling Scheme - PISO
- Spatial Discretisation; Gradient - Least Squares Cell Based, Pressure - PRESTO!, Momentum - Second Order Upwind, Volume Fraction - Compressive, Turbulent Kinetic Energy - Second Order Upwind, Specific Dissipation Rate - Second Order Upwind
- Transient Formulation - First Order Implicit
- Time Step - Initially 0.0001s until model was stable and then increased to 0.001s
- Solution Initialisation - Standard, computed from inlet, Flat open channel initialisation method.

6.5 Revised Polyhedral Meshing

After observing the mesh induced turbulence in both steady-state and transient solutions for the hex dominant mesh models, it was decided to re-mesh the domain using a fully polyhedral mesh. The mesh was refined in the critical areas; the plate, the wake region, and the free surface level. Chapter 5 describes the cell sizes, and the setout of the BOI that were used to refine the mesh in these areas. Boundary conditions used were identical to the model validation simulation with the exception of the sidewalls. ANSYS Fluent reported an error of non matching nodes when trying to establish a translational periodic boundary between to the two side walls. As such these walls were designated as non-slip instead. For all fully polyhedral meshed domains the boundary conditions were as follows: Boundary conditions for the validation model were as follows:

- Pressure inlet with 0.5m.s^{-1} air and liquid fluid velocity
- No-slip wall on the side walls of the domain
- No-slip wall on the bottom of the domain and the surfaces of the plate
- Zero gauge pressure outlet on the top of the domain to simulate the atmosphere
- Zero gauge pressure outlet at the end of the domain to allow the fluids to freely exit the domain

6.6 Chapter Summary

This chapter has presented to the reader the domain size, and plate geometry that was used in the simulations. It also described the method of meshing the domain, the boundary conditions used for initialising the simulations, and the solver settings used.

Chapter 7

Results

7.1 Chapter Overview

This chapter delivers and describes the results of the CFD models completed on the USQ HPC. It also discusses the behaviour of the models during simulation, and provides some comparisons between the models. Information in this chapter is the basis of the comments in the concluding chapter.

7.2 Flat Plates - Full Polyhedral Mesh Model

As the model validation did not go as expected, direct quantitative comparisons to Attiya et al. (2019) results could not be made from the simulations run on ANSYS for this project. The plain flat plates of varying aspect ratios, 0.25, 0.5, and 1 were remodelled using a fully polyhedral mesh. Boundary conditions and solver settings were identical to full hex mesh model, except for the periodic boundary condition which was incompatible with the unstructured mesh. The fully polyhedral mesh was more stable than the hex dominant mesh and only needed to be under relaxed by a factor of 0.5 to remain stable.

The general flow characteristics of the fluid flow over the flat plates can be seen from figures 7.1, 7.2, 7.3, 7.4, 7.5, and 7.6 which show the phases of water (A), normalised Q criterion (B), and magnitude of vorticity (C), in the fluid from the side and top views of the 250, 500, and 1000 wide flat plates. The 250 wide plate in figures 7.1, 7.2, had

a higher concentration of air entrained downstream although the distance to which this persisted was approximately the same for all plate widths.

Coherent Eulerian vortical structures are shown in the figures to be shedding from the sides and bottom edges of the plates. The direction of vortex rotations being back in towards the plate, creating clockwise rotations from the left edge and counter-clockwise rotations from the right edge when viewing the late from the inlet. Vortices in the air phase were shown at the free surface level, and to a lesser extent in the water phase at the domain inlet. The turbulence at the free surface level located at pressure inlet is a result of the Dirichlet pressure inlet condition. Similarly to the entrainment of air, the presence of coherent vortical structures existed for a fairly consistent period of time downstream from the plates regardless of plate widths.

The vorticity magnitude shows that as the plate width is increased, the vorticity magnitude increases in the flow downstream of the plate. The vorticity is much closer to the rear of the plate, and the vorticity continues further downstream with increasing width also. A central channel of reduced turbulence can be shown developing as the plate width increases from 250 to 500W as the vortices shed from the edge of plate are no-longer close enough to interact with each other.

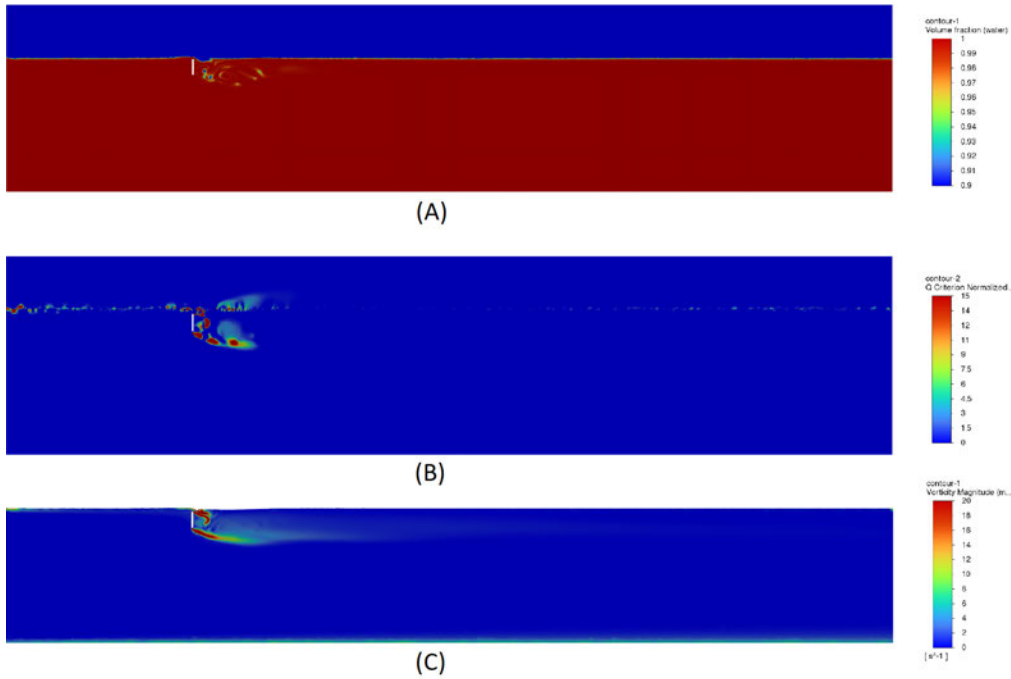


Figure 7.1: View from the Z axis direction of the 250W flat plate (A) Phases volume fraction, (B) Normalised Q Criterion, (C) Vorticity Magnitude.

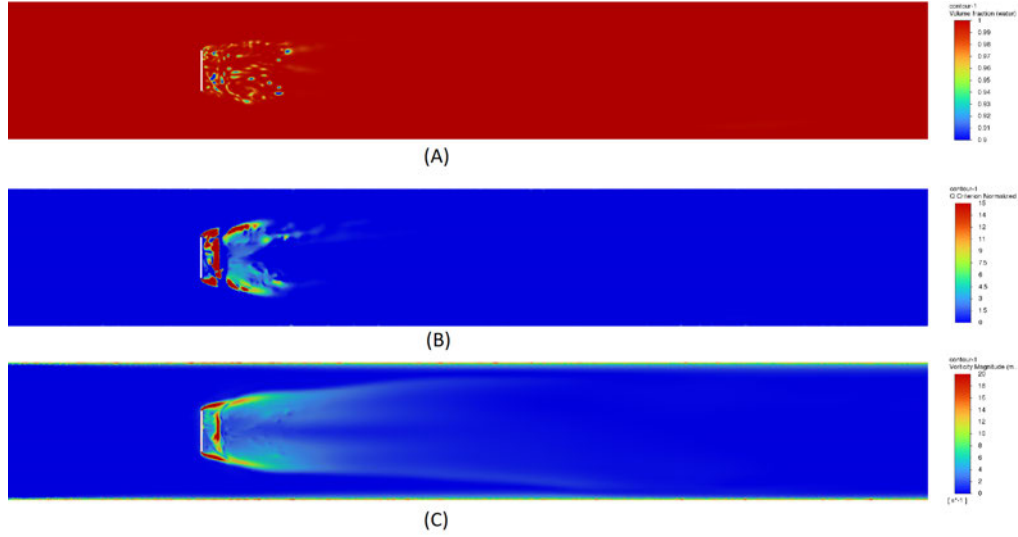


Figure 7.2: View from the Y axis direction of the 250W flat plate (A) Phases volume fraction, (B) Normalised Q Criterion, (C) Vorticity Magnitude.

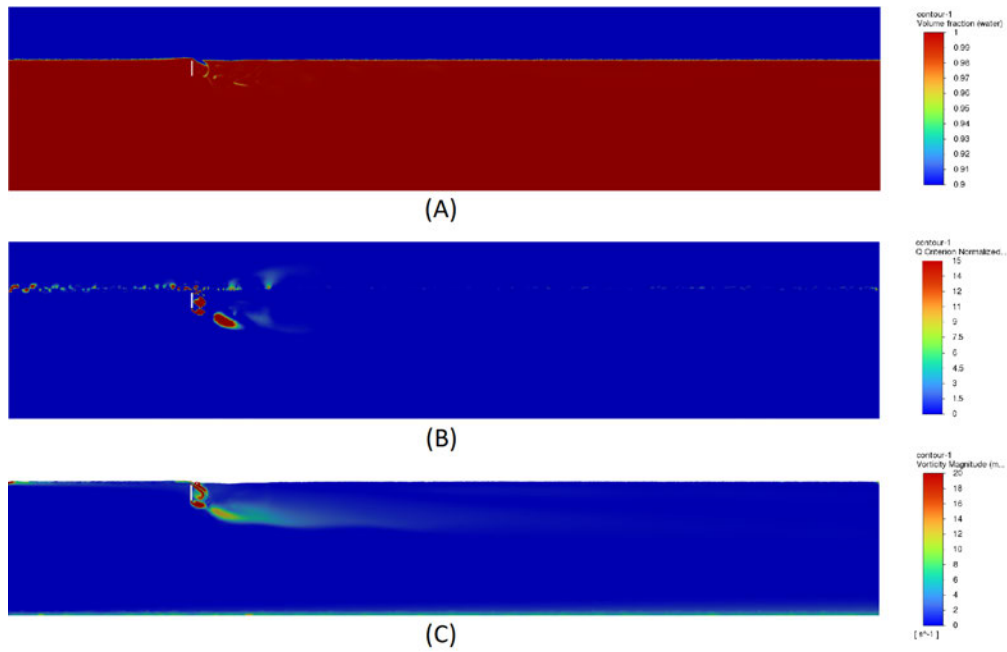


Figure 7.3: View from the Z axis direction of the 500W flat plate (A) Phases volume fraction, (B) Normalised Q Criterion, (C) Vorticity Magnitude.

7.2.1 Flat Plates - Full Polyhedral Mesh Results

The results of the flat simulations with a full polyhedral mesh are show in table 7.1. The average dimensionless wall y plus value was between 1.59 and 1.90 for each plate, indicating that the boundary layer was adequately captured on the plates. Coefficient of drag increased by 5.2% from the 250 to 500 wide plate results and increased by 9.8% from

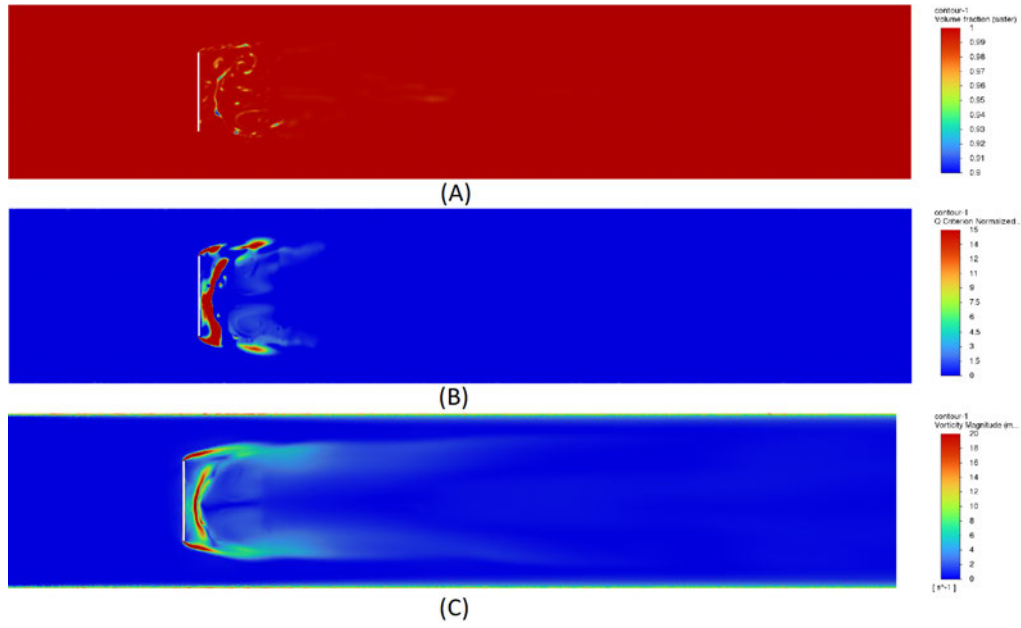


Figure 7.4: View from the Y axis direction of the 500W flat plate (A) Phases volume fraction, (B) Normalised Q Criterion, (C) Vorticity Magnitude.

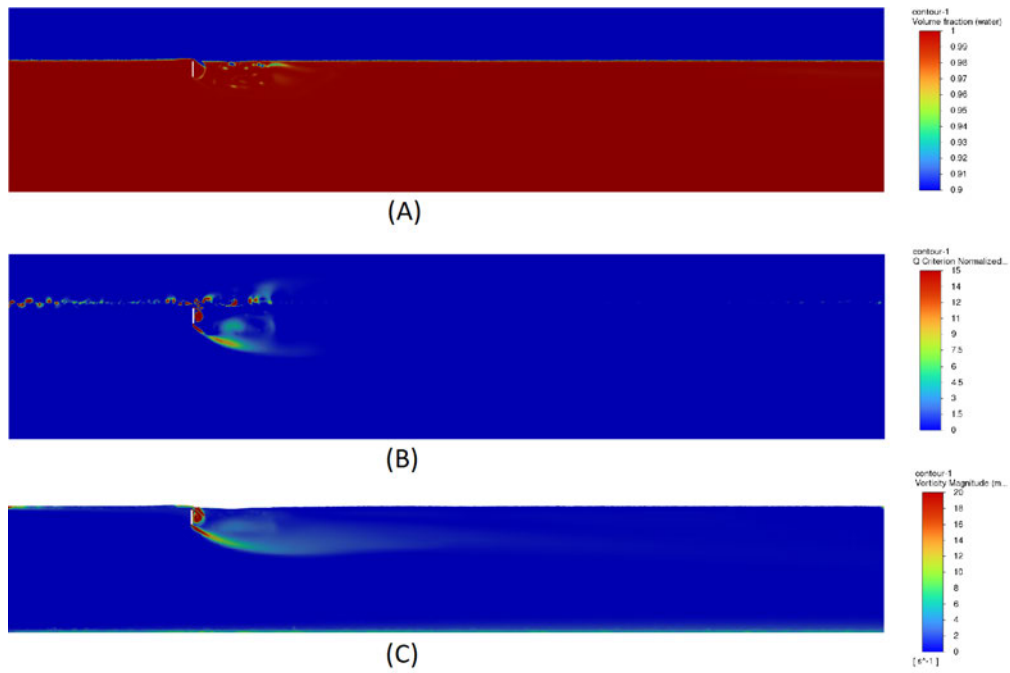


Figure 7.5: View from the Z axis direction of the 1000W flat plate (A) Phases volume fraction, (B) Normalised Q Criterion, (C) Vorticity Magnitude.

the 500 to 1000 wide plate results.

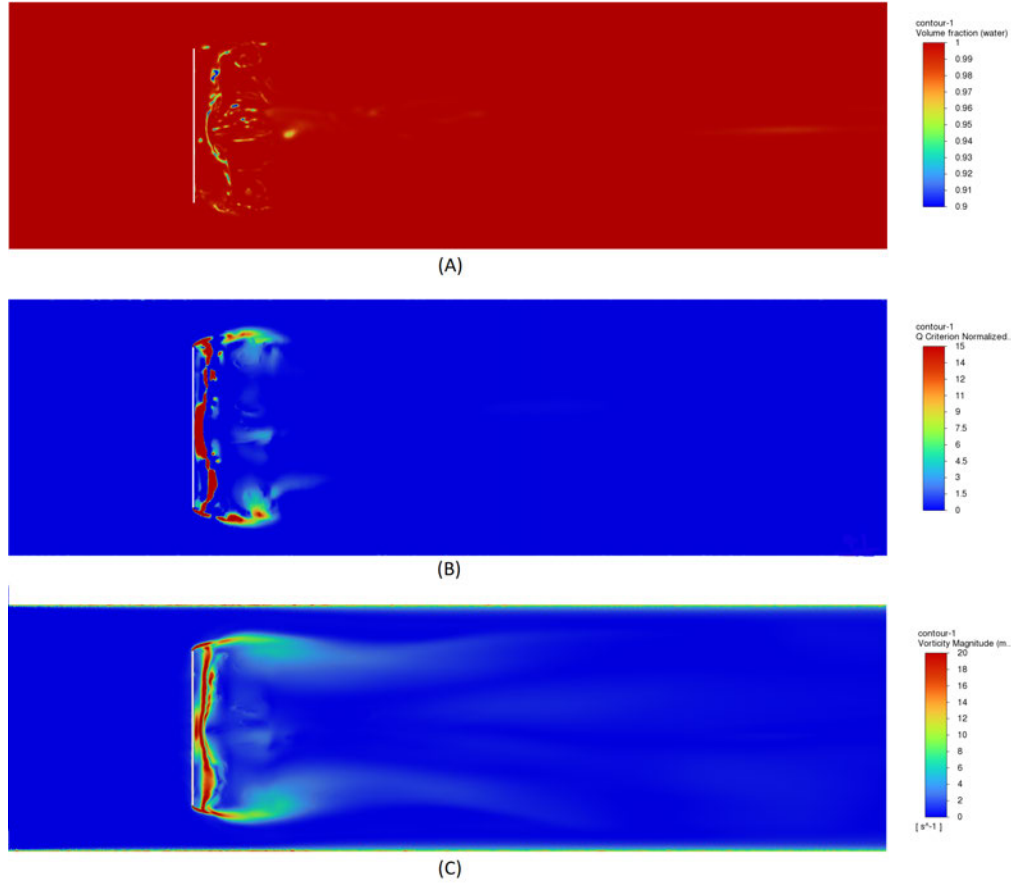


Figure 7.6: View from the Y axis direction of the 1000W flat plate (A) Phases volume fraction, (B) Normalised Q Criterion, (C) Vorticity Magnitude.

Table 7.1: Flat plates with full polyhedral mesh results.

	F_d (N)	F_l (N)	Y+	C_d	C_l
250W Plate	4.2237	2.5014	1.2018	1.3540	0.8019
500W Plate	8.8999	5.0597	1.5942	1.4266	0.8110
1000W Plate	19.5138	10.3984	1.7411	1.5640	0.8334

7.3 Curved Plates - Full Polyhedral Mesh Model

The general flow characteristics of the fluid flow over the curved plates can be seen from figures 7.7, 7.8, 7.9, 7.10, 7.11, and 7.12 which show the phases of water (A), normalised Q criterion (B), and magnitude of vorticity (C), in the fluid from the side and top views of the 250, 500, and 1000 wide curved plates. Again, consistent distances of air entrainment, and to a lesser extent consistent distances of vortical structures are found downstream of the curved plates.

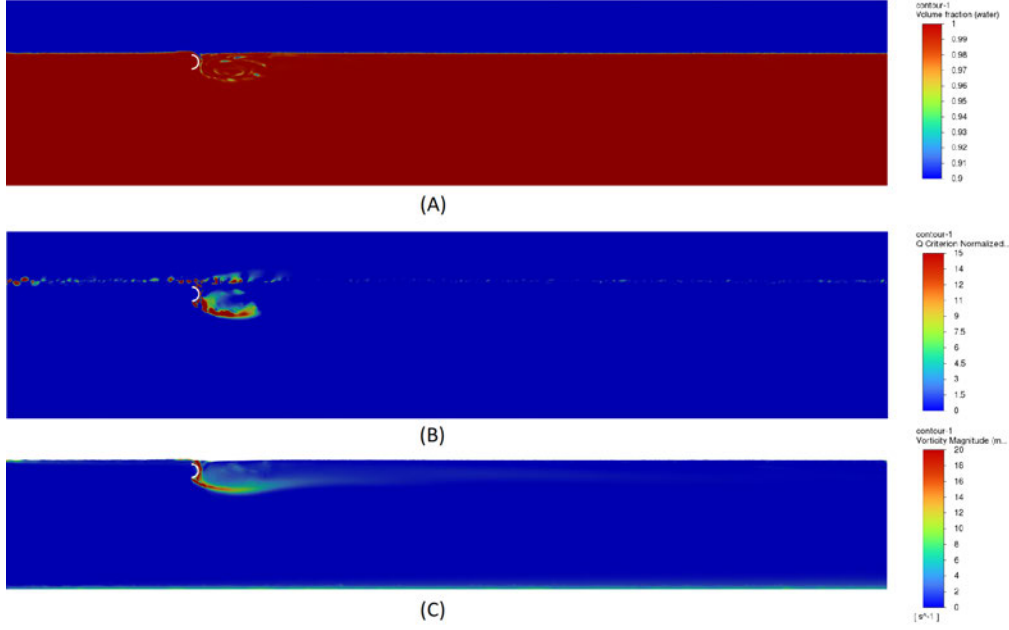


Figure 7.7: View from the Z axis direction of the 250W curved plate (A) Phases volume fraction, (B) Normalised Q Criterion, (C) Vorticity Magnitude.

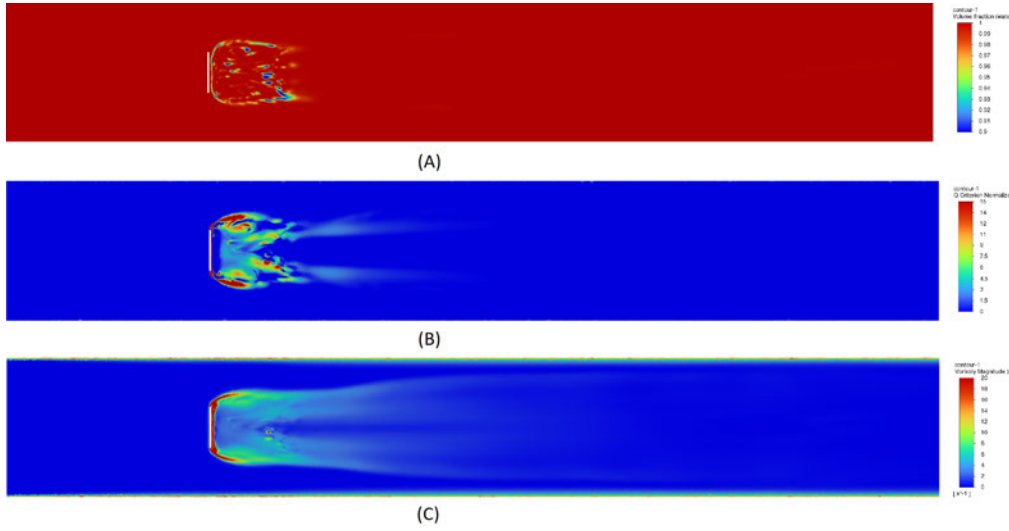


Figure 7.8: View from the Y axis direction of the 250W curved plate (A) Phases volume fraction, (B) Normalised Q Criterion, (C) Vorticity Magnitude.

7.3.1 Curved Plates - Full Polyhedral Mesh Plate Forces

The results of the curved plate simulations with a full polyhedral mesh are shown in table 7.2. The average dimensionless wall y^+ value was between 1.58 and 1.75 for each plate, indicating that the boundary layer was adequately captured on the plates. Coefficient of drag increased by 18.6% from the 250 to 500 wide plate results, but dropped 5.1% from the 500 to 1000 wide plate results.

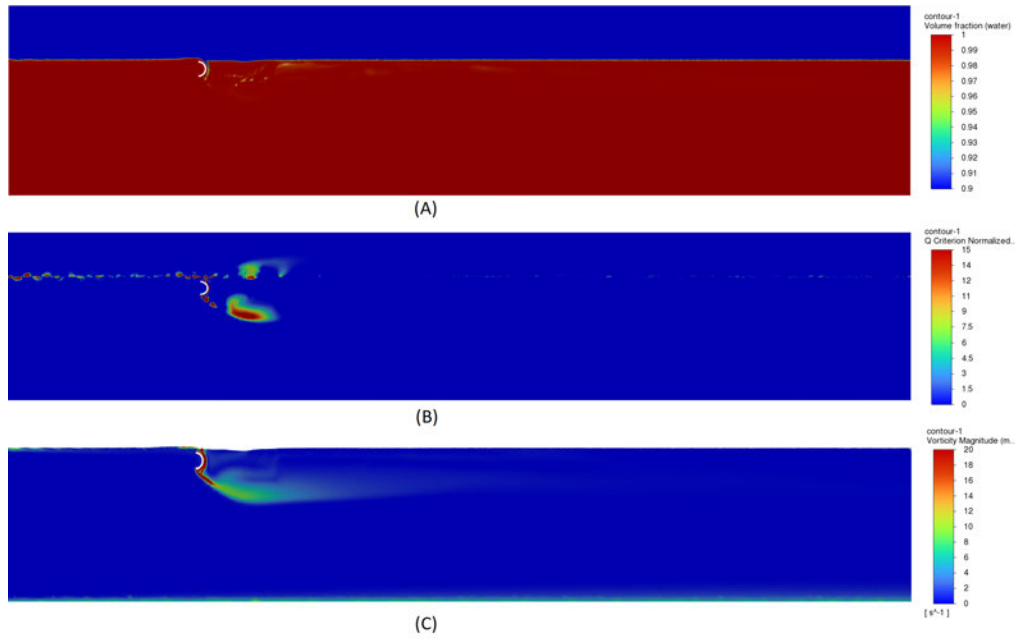


Figure 7.9: View from the Z axis direction of the 500W curved plate (A) Phases volume fraction, (B) Normalised Q Criterion, (C) Vorticity Magnitude.

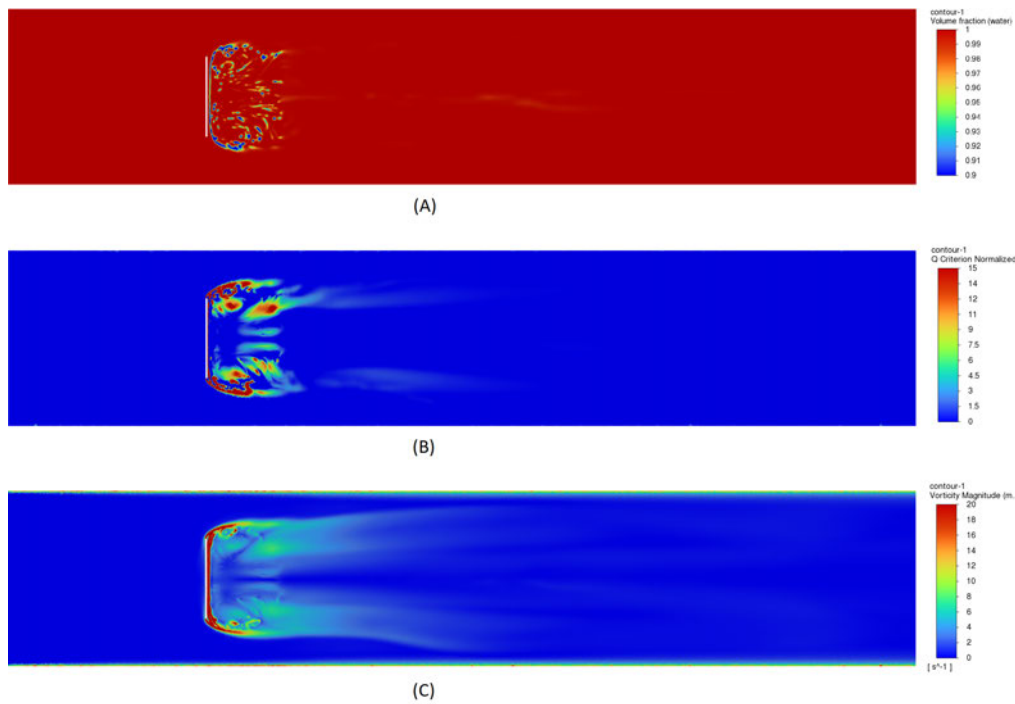


Figure 7.10: View from the Y axis direction of the 500W curved plate (A) Phases volume fraction, (B) Normalised Q Criterion, (C) Vorticity Magnitude.

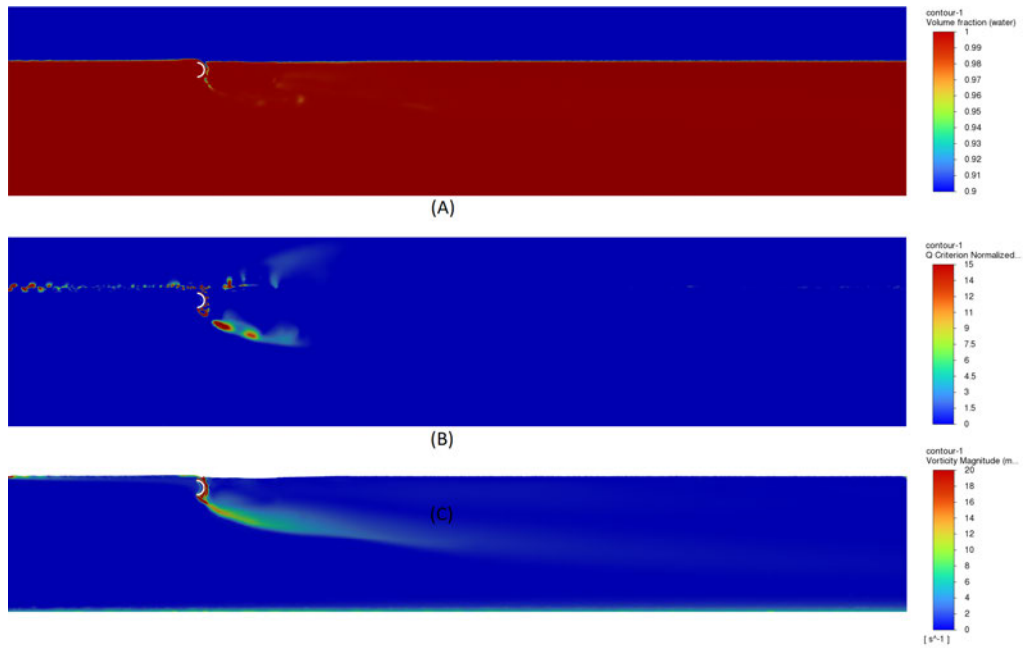


Figure 7.11: View from the Z axis direction of the 1000W curved plate (A) Phases volume fraction, (B) Normalised Q Criterion, (C) Vorticity Magnitude.

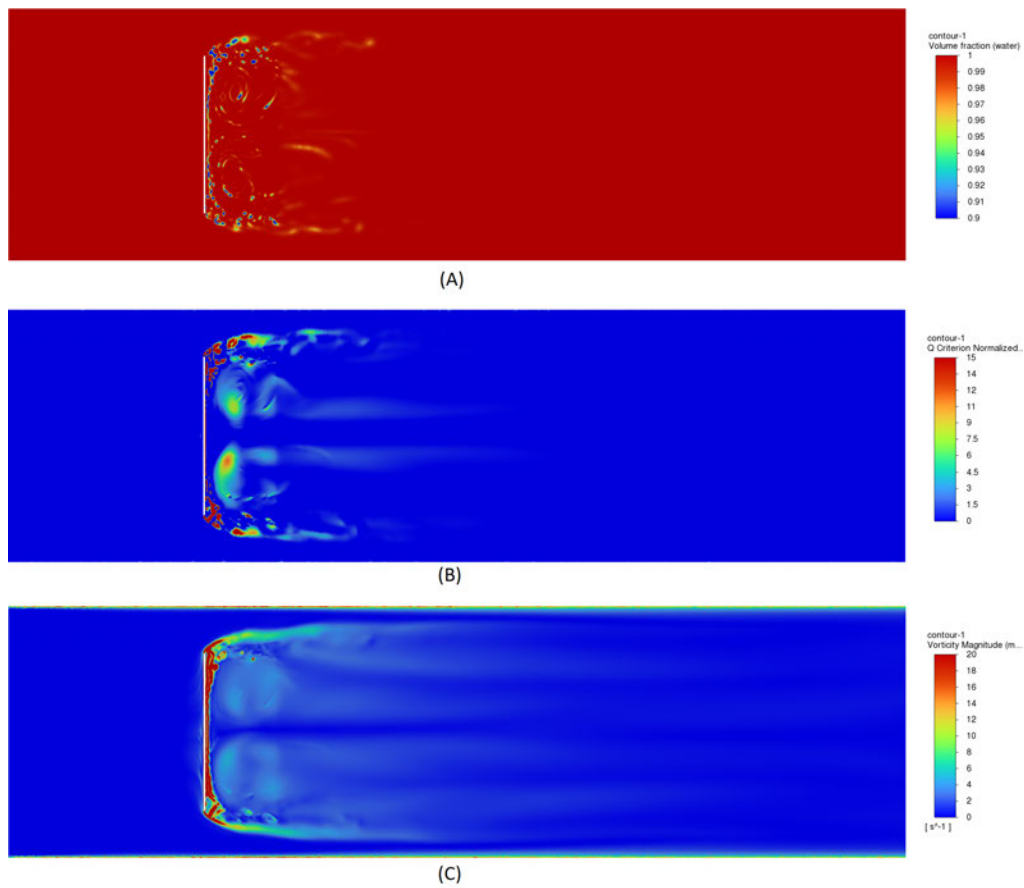


Figure 7.12: View from the Y axis direction of the 1000W curved plate (A) Phases volume fraction, (B) Normalised Q Criterion, (C) Vorticity Magnitude.

Table 7.2: Curved plates with full polyhedral mesh results.

	F_d (N)	F_l (N)	Y+	C_d	C_l
250W Plate	4.5340	4.1763	1.5835	1.4535	1.3388
500W Plate	10.7744	8.3949	1.7316	1.7270	1.3456
1000W Plate	20.6987	16.2504	1.7475	1.6590	1.3024

7.4 Hex Dominant Mesh Model

The Hex Dominant mesh was one of the initial simulations run for the research project. Only a 250mm wide curved plate was simulated using the Hex dominant meshing method. The outer body for hex meshing and inner body for tetrahedral meshing, were combined into a single part in the ANSYS Design Modeller step of the workflow. This ensures that nodal points at the interface of the two spatial regions are common nodes for both the hex and tetrahedral meshes. By having common nodes the transport of the fluxes between the mesh types accuracy is intended to be improved. The simulation was however inherently unstable due to the transition from the hex mesh to the nested tetrahedral mesh. It is believed that the main cause of the instability was the rapid change in volume difference of the cells in the hex mesh, to the pyramid cells in the tetra mesh. In order to allow the simulation to converge, the solution controls had to be under relaxed by a factor of 0.25 which was twice as relaxed as that of the fully polyhedral meshes simulations. Shown in 7.13 there is a ghosting of vorticity in the exact rectangular volume of the nested tetrahedral mesh volume. Based on this false vorticity in the flow, it was decided to use full polyhedral meshing for the rest of the works of the research project.

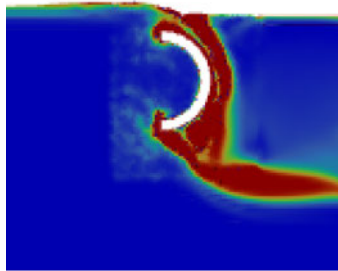


Figure 7.13: Close up of the false vortical flow due to rapid cell volume change in the mesh.

Despite being an erroneous result, the simulation was included in this report to communicate the reasoning behind the decision to change from a hex dominant mesh to a full polyhedral mesh. This simulation was also included as this was the only simulation to utilise the periodic boundary on the side walls. Effects of the periodic boundary can be seen in the y axis views of figure 7.15 with vorticity leaving / entering opposing sides of the domain. Figure 7.14 shows the flow characteristics from the Z axis direction.

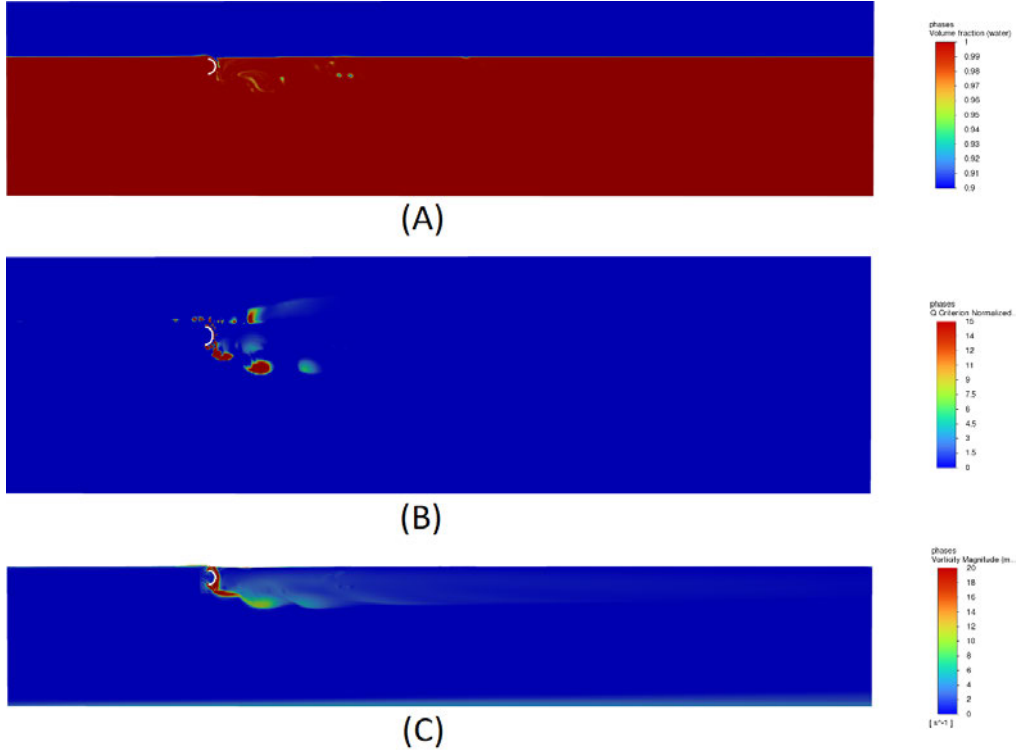


Figure 7.14: View from the Z axis direction of the (A) Phases volume fraction, (B) Normalised Q Criterion, (C) Vorticity Magnitude.

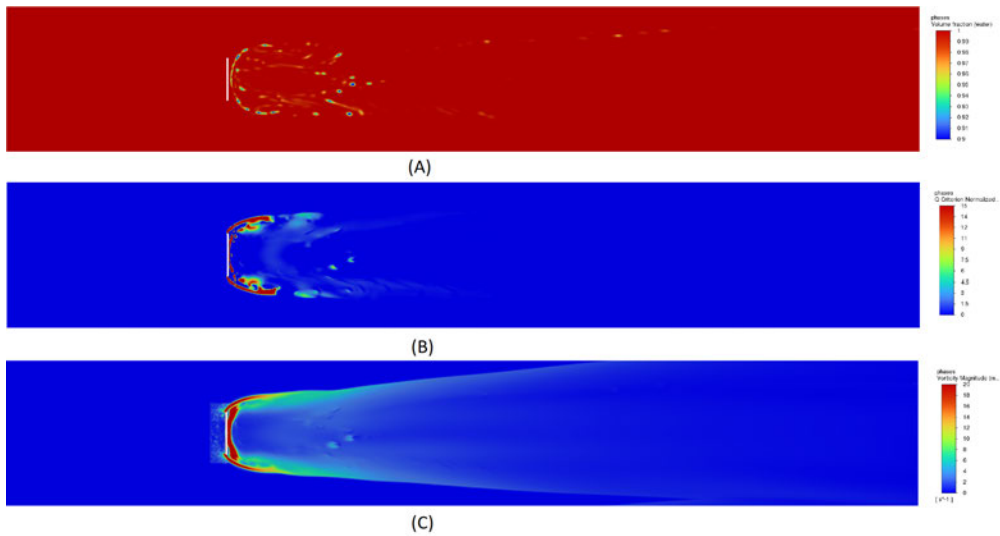


Figure 7.15: View from the Y axis direction of the (A) Phases volume fraction, (B) Normalised Q Criterion, (C) Vorticity Magnitude.

7.4.1 Hex Dominant Mesh Results

The 250 wide curved plate resulted in having an increase of 6.39% and 54.80% in the drag and lift force coefficients acting on the plate respectively, when compared to the results of the validation simulation. While the results in table 7.3 must be take with a grain of

salt due to the false vorticity. Although potentially erroneous, it was promising to see an increase in drag force here, and will provide an interesting comparison to the results of the full polyhedral mesh.

Table 7.3: 250 wide plate results with Hex dominant mesh.

F_D (N)	F_L (N)	Y_+	C_D	C_L
4.6194	3.9257	1.9016	1.481	1.2585

7.5 Transient Model Hex Dominant Mesh Results

The literature indicated that a transient solver with a sufficiently small time step would aid stability and improve accuracy of a solution. Before abandoning the use of the hex dominant mesh type, a URANS method was used to see if this would eliminate the false turbulence at the mesh transition. During initialisation of the model, while it's inherently unstable, the time step used was very small 0.0001 (s). As the solver progressed, each time step was converging within a few iterations so the time step was increased to 0.001 (s). This caused the solver to converge each time step in 10-15 iterations which was a good compromise between compute time and solution time progression.

Figures 7.16 and 7.17 shows the flow characteristics from the Z axis and Y axis direction respectively for the phases of water (A), normalised Q criterion (B), and magnitude of vorticity (C). Figure 7.17 in particular shows more well defined regions of coherent structures using the normalised Q criterion. Unfortunately the turbulence was still present at the transition from hex to tetra mesh regions.

7.5.1 Transient Plate Forces

The time dependent solution showed how the fluid flow and forces acting on the plate varied over time. Figure 7.18 shows the drag force acting on the plate. The drag force is initially unsteady with the initialisation of the model before settling into Kamran vortex shedding behaviour after approximately 5.5 seconds. According to the Karman vortex street formula, eqn 7.1, the frequency of the vortex shedding is 0.989 Hz. Using the peaks of the drag force over the last two full periods of behaviour, the simulation was operating a frequency of 1.044 Hz, which is within 5.5% of the theoretical value.

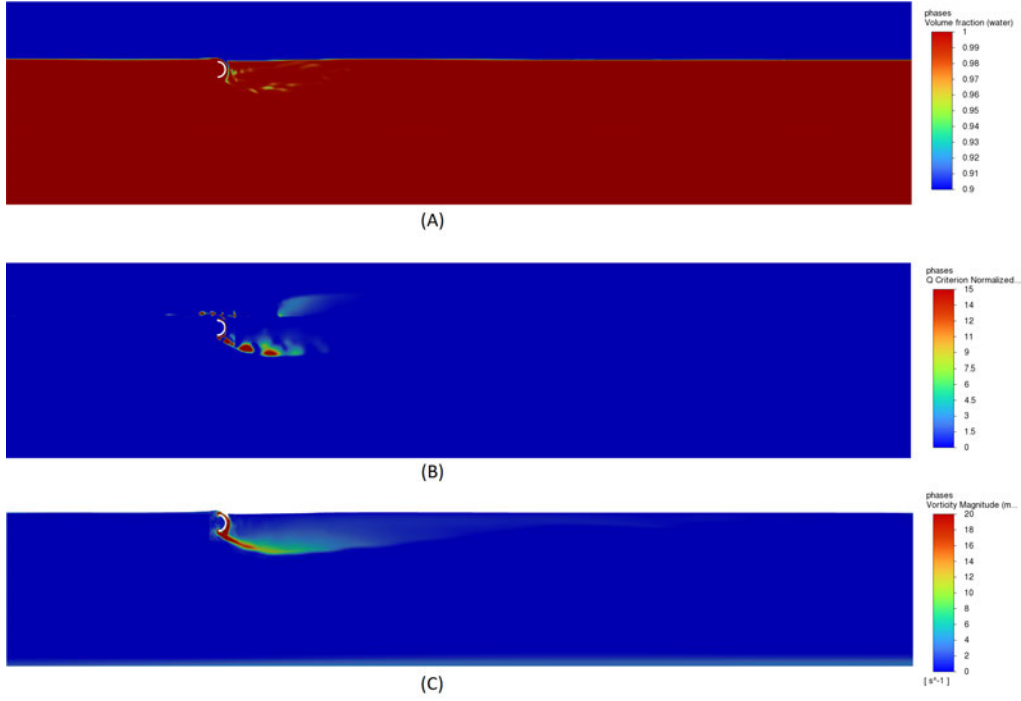


Figure 7.16: Transient Solver View from the Z axis direction of the 250W curved plate (A) Phases volume fraction, (B) Normalised Q Criterion, (C) Vorticity Magnitude.

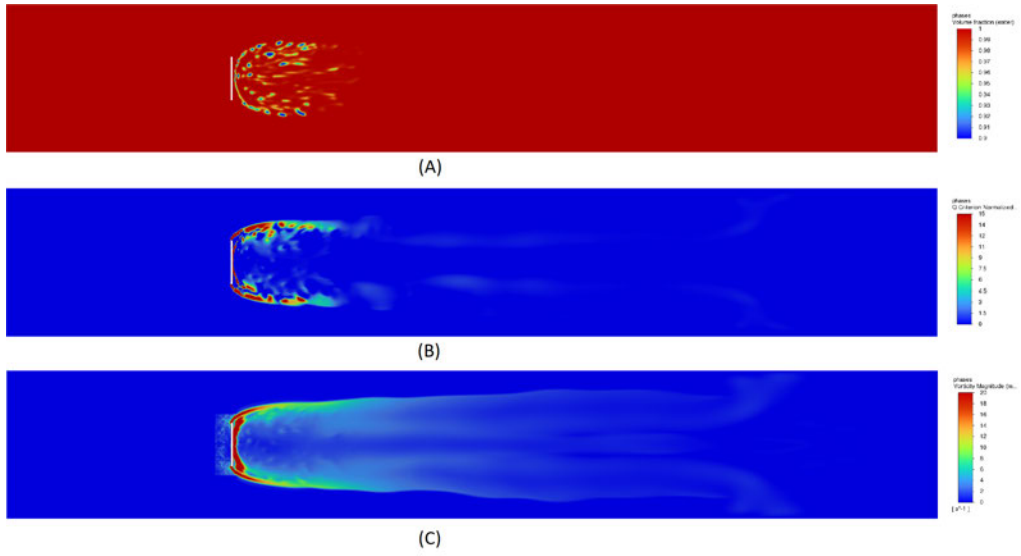


Figure 7.17: Transient Solver View from the Y axis direction of the 250W curved plate (A) Phases volume fraction, (B) Normalised Q Criterion, (C) Vorticity Magnitude.

$$\frac{f \cdot d}{V} = 0.198 \cdot \left(1 - \frac{19.7}{Re}\right) \quad (7.1)$$

The forces over the last two periods were averaged to produce the results shown in table 7.4

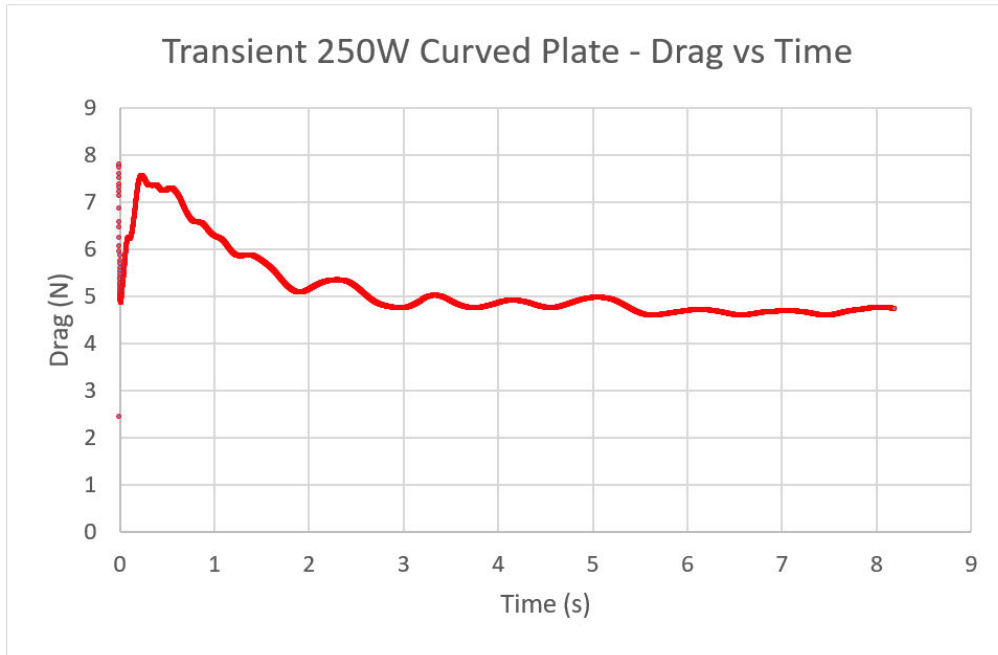


Figure 7.18: Drag forces acting on a 250 wide curved plate over time.

Table 7.4: 250 wide curved plate results from transient solver.

F_D (N)	F_L (N)	Y+	C_D	C_L
4.6529	3.866	1.8233	1.4916	1.2394

7.6 Chapter Summary

This chapter has presented the results of the simulations completed as part of the research project, as defined in Chapters 5 and 6. It includes simulation results for both flat and curved plates of 250, 500, and 1000mm wide plates using polyhedral mesh types, and unsuccessful attempts with a hex dominant mesh. The results have shown the coherent vortical structure behaviour and documented the forces acting on the submerged plates, which will be used in Chapter 8 for discussion.

Chapter 8

Results

8.1 Chapter Overview

This chapter discusses and compares the results of the flat and curved plate simulations. It discusses the similarities and differences of the results and the reasons for these differences. This is the penultimate chapter of the research project and will be the basis for most of the concluding discussions in the final chapter.

8.2 Flat Plate Results vs B. Attiya

B. Attiya reported mean drag co-efficient for the 250, 500, and 1000 wide flat plates as 1.88, 1.79, and 1.73 respectively. Comparing these results to those obtained from the ANSYS Fluent full polyhedral mesh simulation of 1.35, 1.43, and 1.56 we notice two things. Firstly, the results from the polyhedral mesh were significantly lower than those of B. Attiya. Secondly, there was a general trend of the co-efficient of drag increasing with width while B. Attiya showed a decreasing trend.

The cause of reduced co-efficient of drag can be attributed partially to the differences in accuracy of LES and RANS method. If we look at the amount of exposure to air at the back of the plate in (A) of figure 8.1, we can see that B. Attiya had periods where large amounts of the surface area of the plate exposed to air. Juxtaposed to the results of the results of this study which shows the air entrainment moving down and away from the

plate. This is most likely caused by the time average behaviour of the ANSYS simulation. Large amounts of exposure to air on the rear of the plate would significantly reduce the amount of pressure acting on the area, and in turn increase the amount of drag force experienced by the plate.

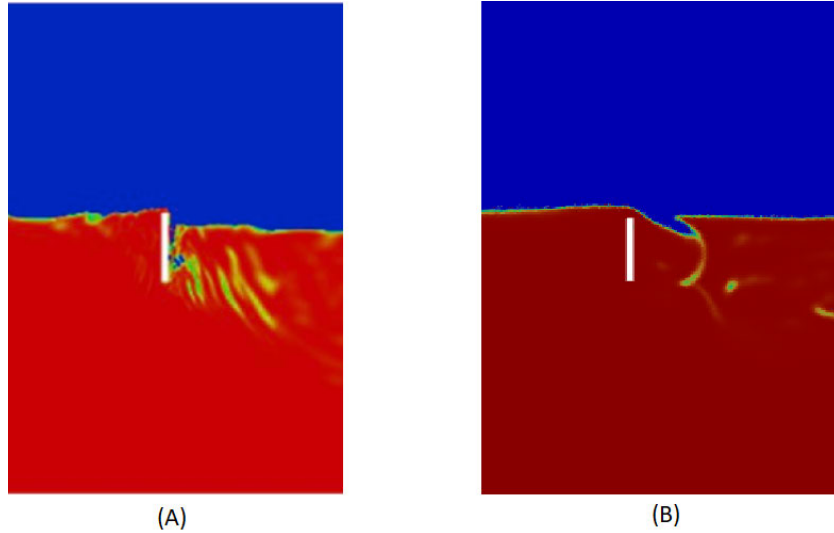


Figure 8.1: Phases of air and water for 500W flat plate from (A) reference literature, and (B) ANSYS full polyhedral simulation.

B. Attiya speculated that the co-efficient of drag decreased with increased plate width due to the free surface shedding larger and more energetic vortices upstream of the plate. These vortices would reduce the amount of pressure on the frontal area of the plate, and decrease the drag force. This behaviour of free surface vortex shedding was far less pronounced in the ANSYS simulations. Only a small layer of vortical velocity was shown under the free surface layer, approximately 15-20mm, and never developed to the full face of the plate. The ANSYS model did show increasing vortical action at the rear of the plate with larger, more energetic coherent structures that were attached to a larger surface area of the plate. Larger vortical structures at the rear of the plate created a larger pressure differential between the front and rear of the plate, increasing the drag force and co-efficient of drag for the wider plates.

8.3 Flat vs Curved Plates

The resulting forces and coefficients of drag and lift for the full polyhedral mesh simulations are given in table 8.1. The 500 wide curved plate had the most significant increase in the co-efficient of drag when comparing the flat to curved plates with a 21% increase, whilst the 250 and 1000 wide plates were only moderate increases of 7.35 and 6.07% respectively. All curved plates had significant increases in lift force ranging from approx 56-67%.

Table 8.1: Flat vs Curved plate forces comparison.

	F_d (N)	F_l (N)	C_d	C_l
FLAT 250W PLATE	4.2237	2.5014	1.354	0.8019
CURVED 250W PLATE	4.534	4.1763	1.4535	1.3388
DIFFERENCE %	7.35	66.96	7.35	66.95
FLAT 500W PLATE	8.8999	5.0597	1.4266	0.811
CURVED 500W PLATE	10.7744	8.3949	1.727	1.3456
DIFFERENCE %	21.06	65.92	21.06	65.92
FLAT 1000W PLATE	19.5138	10.3984	1.564	0.8334
CURVED 1000W PLATE	20.6987	16.2504	1.659	1.3024
DIFFERENCE %	6.07	56.28	6.07	56.28

By examining the vorticity at the plates we can get an understanding of the increase in drag function of the curved plate. Due to the geometry of the curved plate, as water flows over the top edge of the plate, the gradual curve of the plate prevents flow separation at the top edge of the plate. In figure 8.2 it is shown that the vortical flow is adhered to the surface of the plate for virtually the full extent of the rear surface of the plate. By comparison the flat plate sheds vortices from the top edge. With the 1000W flat plate having the strongest and most extensive vortices behind the plate, this reduced the geometrical driven drag gains of the 1000 wide curved plate. The extent and persistence of the vortical structures appears to be slightly larger for the curved plates when looking at the normalised vorticity and Q criterion plots in Chapter 7.

The significant increase in lift force can be attributed to the geometric properties of the plates. The curved plates have a larger surface area that the vertical component of that the fluid pressure can act on. This results in a larger differential between the vertical pressure forces on the plate.

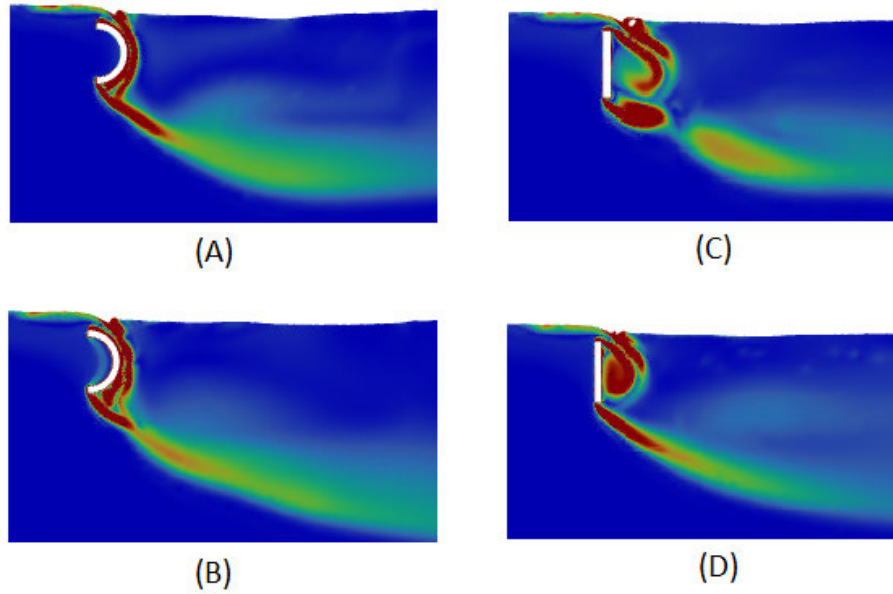


Figure 8.2: Normalised vorticity comparison of the (A) 500 wide curved plate and (B) 1000 wide curved plate to the (C) 500 wide flat plate and (D) 1000 wide flat plate.

8.4 Steady State vs Transient 250W Flat Plate

The transient solver solution showed the Karman vortex shedding behaviour that is typical in flows around an object. This behaviour is lost in a typical steady-state solver solution. Periodic results were obtained and the average co-efficient of drag over two periods 1.49, varied by 2.76% to the steady state solution of 1.45m which is considered good agreement. Observing the normalised vorticity magnitude and Q criterion plots for these simulations the higher resolution of turbulent flow can be seen in the transient solution. Where the steady-state plots tend to have larger and broadly defined areas of turbulence, the transient plots show smaller but more dense and well defined areas of turbulence.

8.5 Chapter Summary

This chapter has discussed the results presented in Chapter 7. A comparison between the results of the flat and curved plate forces was made showing an increase in drag and lift co-efficients of the curved plate. The reasons for the differences was also discussed, attributing the additional drag force to the adhesion of the vortex layer to the rear of the curved plate. Differences between the steady state and transient solver solutions was lightly touched on, as this was not the primary focus of the research paper, and the

presence of what appears to be mesh induced turbulence may be affecting the results.

Chapter 9

Conclusions and Further Work

9.1 Conclusions

The motivation for the project was to investigate the potential to increase the efficiency of linear energy harvester devices through geometric changes to the plate design. Originally intended to build upon the works of (Attiya et al. 2019) which studied the effects of varying flat plate aspect ratios, the project aims had to be updated when model validation could not be achieved. The project then sought to produce it's own results for both flat and curved plates in order to compare them to one another. This involved using ANSYS Fluent to simulate submerged flat and curved plates in a domain of full polyhedral cells.

Determining the appropriate domain size and cell refinement for domain independent results was done systematically. The plates were then simulated using a steady-state solver to produce results for analysis. It was found that for a 250, 500, and 1000mm wide by 100mm high flat plates, by adding a 50mm radius bend to the plate the co-efficients of lift and drag were increased. On the 250 wide plate the drag was increased by 7.35%, the 500 wide plate 21.06%, and the 1000 wide plate 6.07% by adding a curve to the plate. All plates experienced large increases in lift ranging from 56.3 to 67.0%.

It was shown that the main cause for the increase in the drag force acting on the plate was due to the turbulent flow generated off the plate surface. In the case of the flat plates, the vortices were shed at the rear of the top of edge and flowed down and away from the plate. Comparatively the curved plates vortices flowed down nearly the full extent of

the rear face of the plate before interacting with the bottom edge vortices and shedding into the fluid. This vortical flow lowers the fluid pressure on the rear of the plate which increases the drag force acting on the plate.

Whilst comparing results from a validated model would have been ideal, this research project has shown that by changing the geometry of a submerged plate, the performance of a linear energy harvester could potentially be improved. These generators utilise an array of plates so further analysis will be required to definitively quantify the extent of improvement.

9.2 Further Work

Results from this research project showed high potential for the improvement of plate performance. This project was by no means exhaustive however. There is still a broad scope of works that could be completed for future research projects in regards to this topic including:

- **Validate results with experimental data:** The results of the simulation conducted in the project, as well as those conducted by Attiya, could be validated by conducting experiments to measure the forces acting on the submerged plates. This would ensure that the results of the CFD analysis is accurate.
- **Simulate various other geometries:** Other plate geometries could be simulated for further improvements to plate performance. This might include for example, closed ends of the curved plates, different curve profiles, or adding roughness to the surfaces.
- **Large Eddy Simulation of curved plate:** More advanced and accurate methods of CFD analysis could be performed on the plates in a multi-phase flow. This would allow a direct comparison to the works of Attiya.
- **Simulate an array of plates:** An array of plates could be simulated CFD. This would be useful in determining how the flows would interact, and find the ideal spacing of plates in a system.
- **Linear Energy Harvester Analysis:** A general analysis of the potential energy that could be extracted from a fluid flow using a Linear Energy Harvester.

9.3 Project Self-Assessment

Overall the research projects success was mildly successful in achieving it's original aims. The model validation process required the project to change it's targets, which were generally achieved. Depth of the analysis of results could also have been improved. Overall though the simulations showed an improvement in the performance of the plates.

There were a few factors affecting the works and outcomes contributing to these short comings. The original reference paper had some discrepancies between the reported mesh and cell sizes. The paper also didn't fully define the inlet conditions and initialisation conditions. To address this contact could have been made with the original author to discuss the model, and or more iterations of simulations with varying inlet conditions performed until the model was validated.

Finally, due to external factors, works could not begin on the project until week 14 of the first semester 2023. Unfortunately this was unavoidable. This reduced the amount of time to complete the project which proved very challenging due to unfamiliarity with both ANSYS and LaTeX software packages. It resulted in the literature review being completed almost concurrently with performing the CFD analysis. This slowed down the process and led to mistakes being made that could have been avoided.

References

- Akan, A. (2006), *Open Channel Hydraulics*, 1st edn, Elsevier Inc.
- Al-Salami, J., Kamra, M. M. & Hu, C. (2021), ‘A high order flux reconstruction interface capturing method with a phase field preconditioning procedure’, *Journal of Computational Physics* **438**, 110376. DOI: <https://doi.org/10.1016/j.jcp.2021.110376>.
- Alexander, D. (2017), *Nature’s Machines An Introduction To Organismal Biomechanics*, 1st edn, Elsevier Inc.
- Ali, A., Jaber, A., Yaseen, M., Rasheed, M., Bazighifan, O. & Nofal, T. (2022), ‘A comparison of finite difference and finite volume methods with numerical simulations: Burgers equation model’, *Complexity* p. 9. DOI: [10.1155/2022/9367638](https://doi.org/10.1155/2022/9367638).
- Altimemy, M., Attiya, B., Daskiran, C., Liu, I.-H. & Oztekin, A. (2018), Investigation of three-dimensional lagrangian coherent structures in flow past single and arrays of plate: Linear energy harvesting applications. DOI: [10.1115/IMECE2018-86332](https://doi.org/10.1115/IMECE2018-86332).
- Anderson, J. (1995), *Computational Fluid Dynamics: The Basics with Applications*, 1st edn, McGraw-Hill Inc.
- Ansys (2010), ‘Ansys fluent user’s guide R13.0’.
- Ansys (2011), ‘Ansys fluent theory guide R14.0’.
- Ansys (2018), ‘Ansys fluent user’s guide R18.1’.
- Asako, Y., Japar, W., Mohamed, S., Sidik, N. & Yusof, S. (2020), ‘A short review on rans turbulence models’, *CFD Letters* **11**, 83–96. DOI: [10.1155/2022/9367638](https://doi.org/10.1155/2022/9367638).
- Attiya, B., Altimemy, M., Caspar, J., Daskiran, C., Liu, I.-H. & Oztekin, A. (2019), ‘Large eddy simulations of multiphase flows past a finite plate near a free surface’,

- Ocean Engineering* **188**, 106342. DOI: [10.1016/j.oceaneng.2019.106342](https://doi.org/10.1016/j.oceaneng.2019.106342).
 URL: <https://www.sciencedirect.com/science/article/pii/S0029801819305050>
- Blazek, J. (2001), *Computational Fluid Dynamics: Principles and Applications*, 1st edn, Elsevier Inc.
- Cengel, Y. & Cimbala, J. (2014), *Fluid Mechanics: Fundamentals and Applications*, 3rd edn, McGraw-Hill Inc.
- Diskin, B. & Thomas, J. (2012), ‘Effects of mesh regularity on accuracy of finite-volume schemes’, *50th AIAA Aerospace Sciences Meeting Including the New Horizons Forum and Aerospace Exposition*. DOI: [.org/10.2514/6.2012-609](https://doi.org/10.2514/6.2012-609).
- Frei, W. (2017), ‘Which turbulence model should i choose for my cfd application’, <https://www.comsol.com/blogs/which-turbulence-model-should-choose-cfd-application/>. [Online; accessed September-2023].
- Gerasimov, A. (2016), Quick guide to setting up les-type simulations, Powerpoint Presentation, ANSYS. https://www.tfd.chalmers.se/~lada/comp_turb_model/postscript_files/Quick_Guide_to_Setting_Up_LES_version_1.4_for_Lars.pdf.
- GREEN, M., Rowley, C. & Haller, G. (2007), ‘Detection of lagrangian coherent structures in three-dimensional turbulence’, *Journal of Fluid Mechanics* **572**, 111 – 120. DOI: [10.1017/S0022112006003648](https://doi.org/10.1017/S0022112006003648).
- Hussain, A. (1986), ‘Coherent structures and turbulence’, *Fluid Mechanics* **173**, 303–356. DOI: [10.1017/S0022112086001192](https://doi.org/10.1017/S0022112086001192).
- Joaquim, P. & Spencer, S. (2005), *Finite Difference, Finite Element and Finite Volume Methods for Partial Differential Equations*, Springer Netherlands, Dordrecht, pp. 2415–2446.
- Katopodes, N. D. (2018), *Free-Surface Flow - Computational Methods*, 1st edn, Elsevier Inc.
- Knupp, P. (2003), ‘Algebraic mesh quality metrics for unstructured initial meshes’, *Finite Elements in Analysis and Design* **39**, 217–241. DOI: [10.1016/S0168-874X\(02\)00070-7](https://doi.org/10.1016/S0168-874X(02)00070-7).

- Knupp, P. (2007), ‘Remarks on mesh quality’, *46th AIAA Aerospace Sciences Meeting and Exhibit*.
- Layton, B. (2008), ‘A comparison of energy densities of prevalent energy sources in units of joules per cubic meter’, *International Journal of Green Energy* pp. 435–455. DOI: [10.1080/15435070802498036](https://doi.org/10.1080/15435070802498036).
- Malalasekera, W. & Versteeg, H. (2007), *An Introduction To Computational Fluid Dynamics: The Finite Volume Method*, 2nd edn, Pearson Education Limited.
- Motsamai, O. S., Muiruri, P. I. & Ndeda, R. (2019), ‘A comparative study of rans-based turbulence models for an upscale wind turbine blade’, *SN Applied Sciences* **1**, 1–15. DOI: [10.1007/s42452-019-0254-5](https://doi.org/10.1007/s42452-019-0254-5).
- Moukalled, F., Mangani, L. & Darwish, M. (2016), *The Finite Volume Method in Computational Fluid Dynamics*, 1st edn, Springer International Publishing.
- Munson, B., Okiishi, T., W.Huebsch & Rothmayer, A. (2013), *Fundamentals of Fluid Mechanics*, 7th edn, John Wiley and Sons Inc.
- NASA (2021a), ‘Boundary layer’, <https://www.grc.nasa.gov/www/k-12/BGP/boundlay.html>. [Online; accessed July-2023].
- NASA (2021b), ‘Navier-stokes equations’, <https://www.grc.nasa.gov/www/k-12/airplane/nseqs.html>. [Online; accessed May-2023].
- OBERKAMPF, W. L. & TRUCANO, T. G. (2002), ‘Verification and validation in computational fluid dynamics’. DOI: [10.2172/793406](https://doi.org/10.2172/793406).
- Peacock, T. & Dabiri, J. (2010), ‘Introduction to Focus Issue: Lagrangian Coherent Structures’, *Chaos: An Interdisciplinary Journal of Nonlinear Science* **20**(1), 017501. DOI: [10.1063/1.3278173](https://doi.org/10.1063/1.3278173).
- Pomraning, E. (2000), Development of Large Eddy Simulation Turbulence Models, PhD thesis, University of Wisconsin, Madison, Wisconsin.
- Pritchard, P. (2013), *Introduction To Fluid Mechanics*, 8th edn, John Wiley and Sons Inc.
- Rehm, B., Schubert, J., Haghshenas, A., Paknejad, A. S. & Hughes, J. (2008), Chapter two - situational problems in mpd, in ‘Managed Pressure Drilling’, Gulf Publishing Company, pp. 39–80. DOI: [10.1016/B978-1-933762-24-1.50008-5](https://doi.org/10.1016/B978-1-933762-24-1.50008-5).

- Rodriguez, S. (2019), *Applied Computational Fluid Dynamics and Turbulence Modeling*, 1st edn, Springer International Publishing.
- SimScale (2022), ‘Periodic boundary condition’, <https://www.simscale.com/docs/simulation-setup/boundary-conditions/periodic-boundary-condition/>. [Online; accessed June-2023].
- SimScale (2023), ‘What is laminar flow’, <https://www.simscale.com/docs/simwiki/cfd-computational-fluid-dynamics/what-is-laminar-flow/>. [Online; accessed June-2023].
- Simulations, I. (2020), ‘Turbulence models in cfd’, <https://www.idealsimulations.com/resources/turbulence-models-in-cfd/>. [Online; accessed Jun-2023].
- Solmaz, S. (2023), ‘Turbulence: Which model should i select for my cfd analysis?’, <https://www.simscale.com/blog/turbulence-cfd-analysis/>. [Online; accessed July-2023].
- Wang, F., Gao, A., Wu, S., Zhu, S., Dai, J. & Liao, Q. (2019), ‘Experimental investigation of coherent vortex structures in a backward-facing step flow’, *Water* **11**(12). DOI: [10.3390/w11122629](https://doi.org/10.3390/w11122629).
URL: <https://www.mdpi.com/2073-4441/11/12/2629>
- Wu, C.-C., Völker, D., Weisbrich, S. & Neitzel, F. (2022), ‘The finite volume method in the context of the finite element method’, *Materials Today: Proceedings* **62**, 2679–2683. 37th Danubia Adria Symposium on Advances in Experimental Mechanics.
URL: <https://www.sciencedirect.com/science/article/pii/S2214785322037804>
- Zhiyin, Y. (2015), ‘Large-eddy simulation: Past, present and the future’, *Chinese Journal of Aeronautics* pp. 11–24. DOI: [10.1016/j.cja.2014.12.007](https://doi.org/10.1016/j.cja.2014.12.007).

Appendix A

Project Specification

ENG4111/4112 Research Project

Project Specification

For: **Stein Anderson**

Title: 3D Simulation of Submerged Plate

Major: Mechanical Engineering

Supervisors: Dr. Khalid Saleh

Enrolment: ENG4111 – EXT S1, 2023

ENG4112 – EXT S2, 2023

Project Aim: To research multiphase flows past various plate shapes with free ends in close proximity to a free surface, and how geometric changes in the plate affect the turbulent flow structures. Through the use of 3D simulation, the analysis of hydrodynamic loadings on the plates shall be refined with the goal of increasing the amount of drag force to the maximum.

Programme: Version 1, 13th March 2023

1. Conduct initial background research on multiphase flows around objects.
2. In depth literature review into the numerical analysis and simulation of multiphase flows, including the use of software package Ansys Fluent.
3. Review previous simulation results and corroborate results using Ansys Fluent.
4. Refine plate design and simulate with rough mesh size on workstation PC.
5. Utilise the HPC to re-run the simulation with a fine mesh size.
6. Report the data from analysis.

If time and resource permit:

7. Investigate different plate designs.
8. ???

Agreed:

Student Name: Stein Anderson

Supervisor Name: Dr. Khalid Saleh

Date: 13/03/2023

Date: TBC

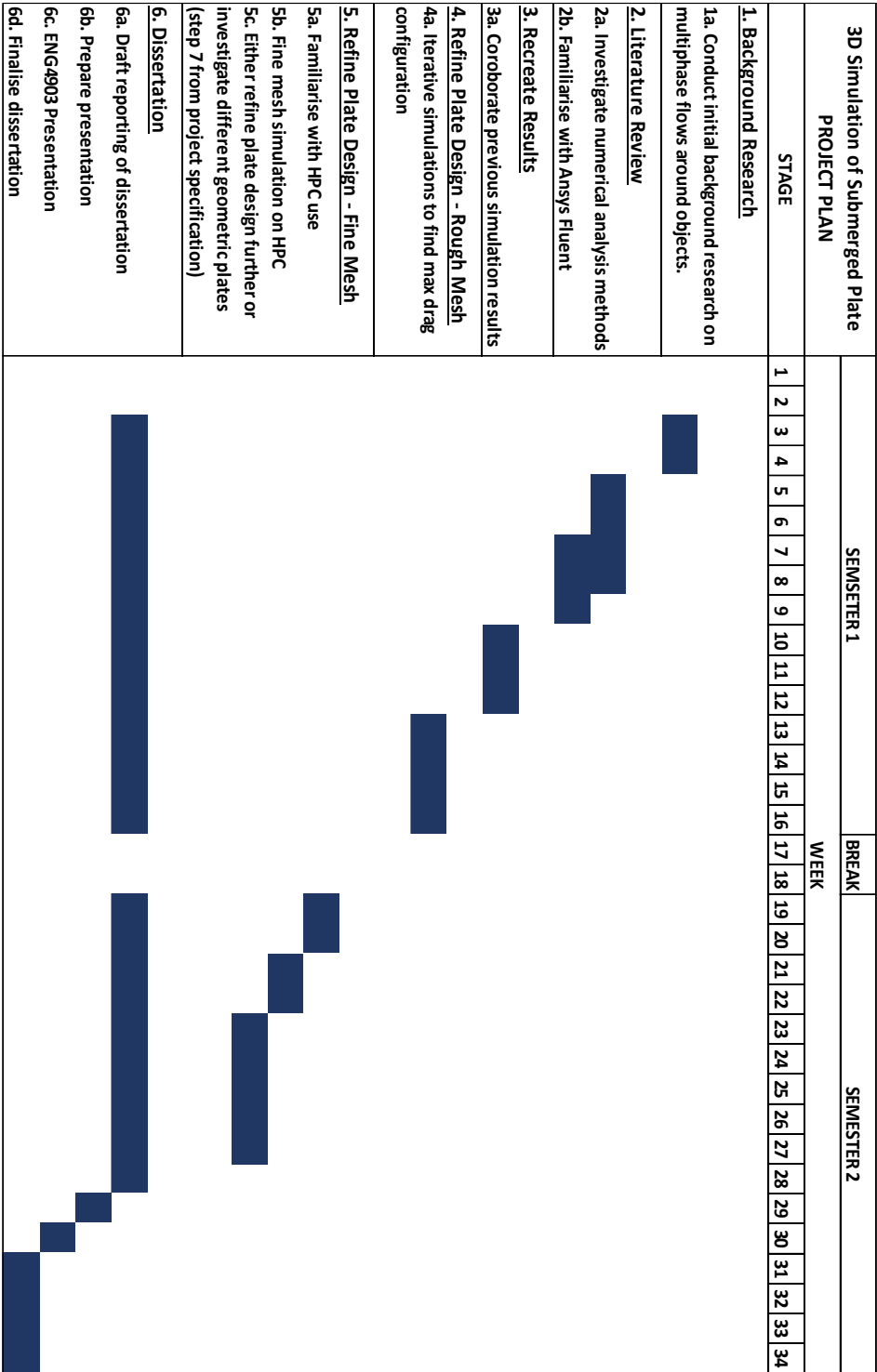
Appendix B

Project Plan

Project Planning

The scheduled stages have been identified as the steps necessary to achieve the aims of the project.

Fortnightly progress update emails with the project supervisor, approx 2 face to face meetings per semester, and online meetings as required.



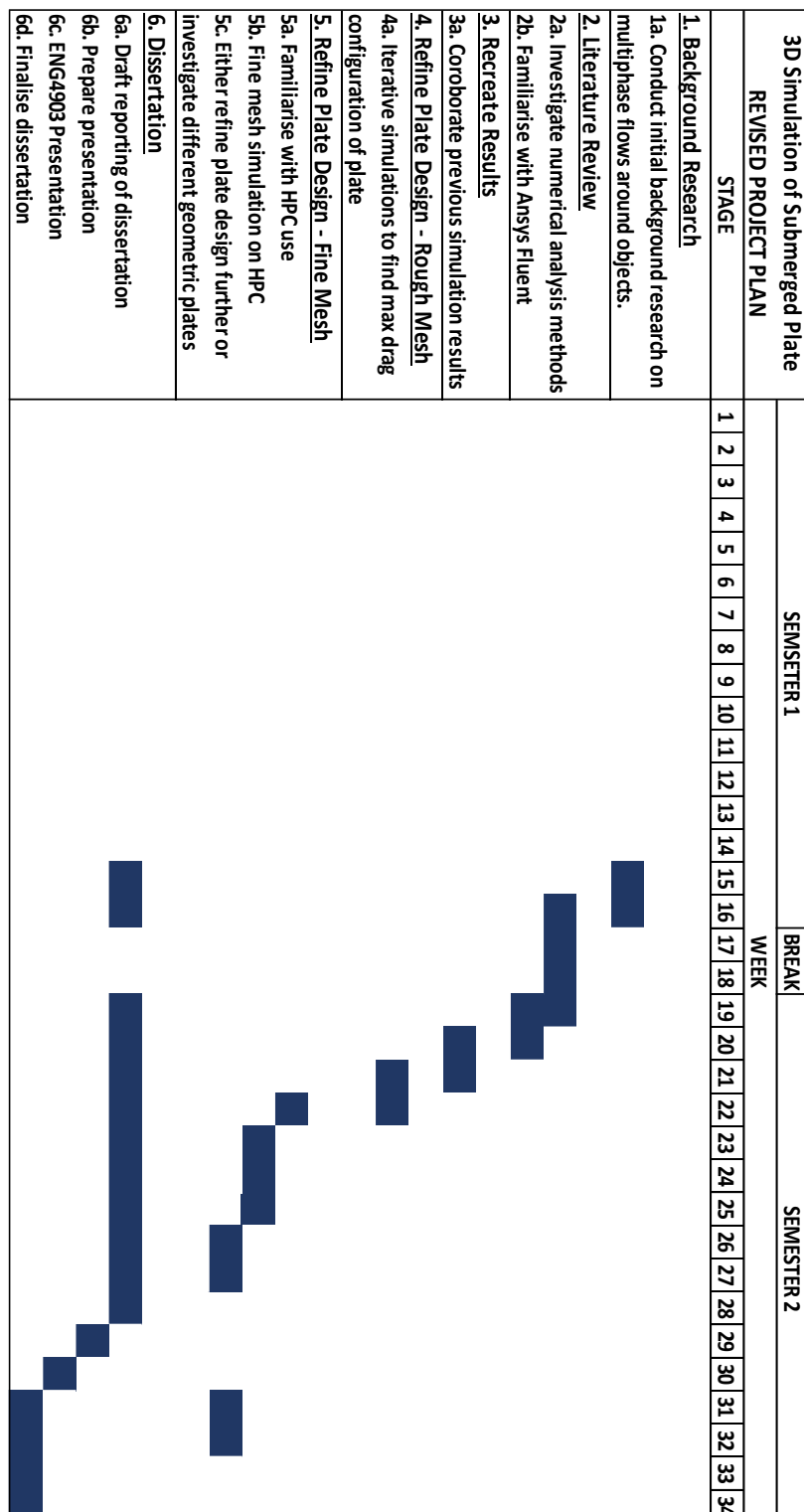
Project Schedule

Appendix C

Revised Project Plan

Project Planning

Due to external factors work on the research project could not commence prior to the last week of May. As such the project plan was updated to suit with shortened task completion targets.



Appendix D

B. Attiya et al. 2019 Drag Results

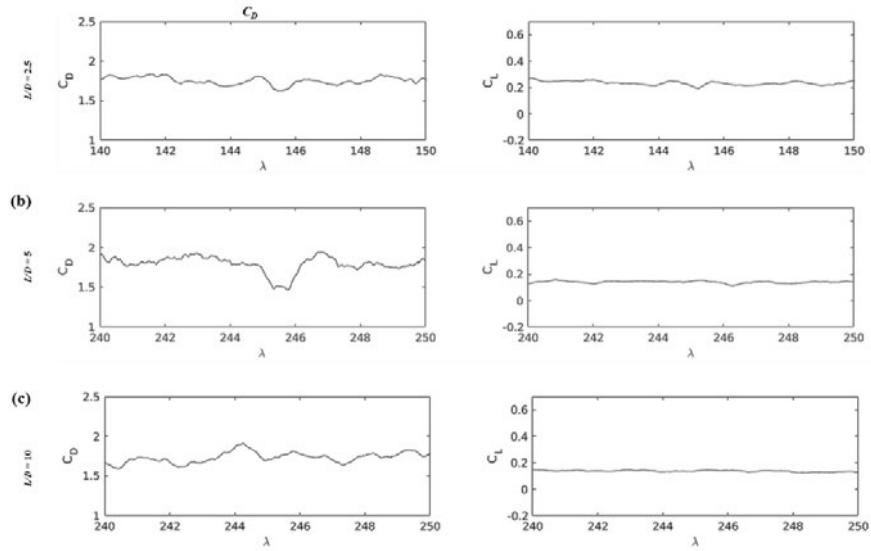


Fig. 14. The drag (left column) and lift (right column) coefficient as a function of time for the plate length (a) $2.5D$, (b) $5D$, and (c) $10D$.

Figure D.1: Drag results from (Attiya et al. 2019)